Multilayer interference coatings

$$m\lambda = 2d \sin \theta$$

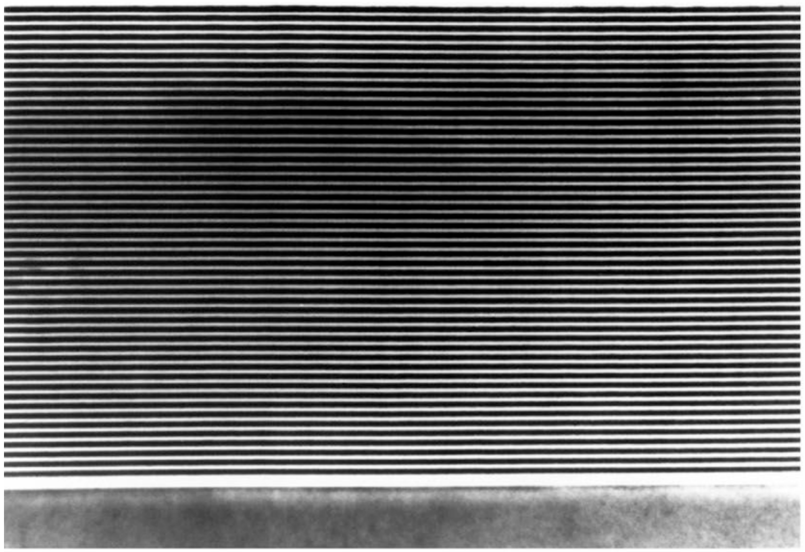

(W/C, T. Nguyen)

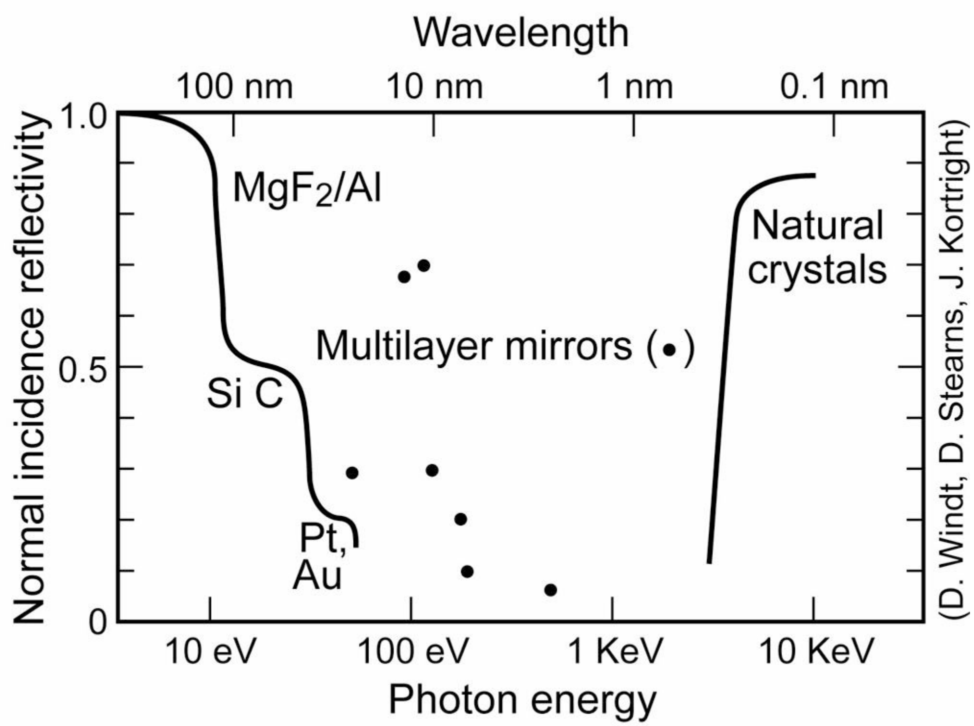

Ch4_F00_Feb2007.ai

Scattering by density variations within a multilayer coating

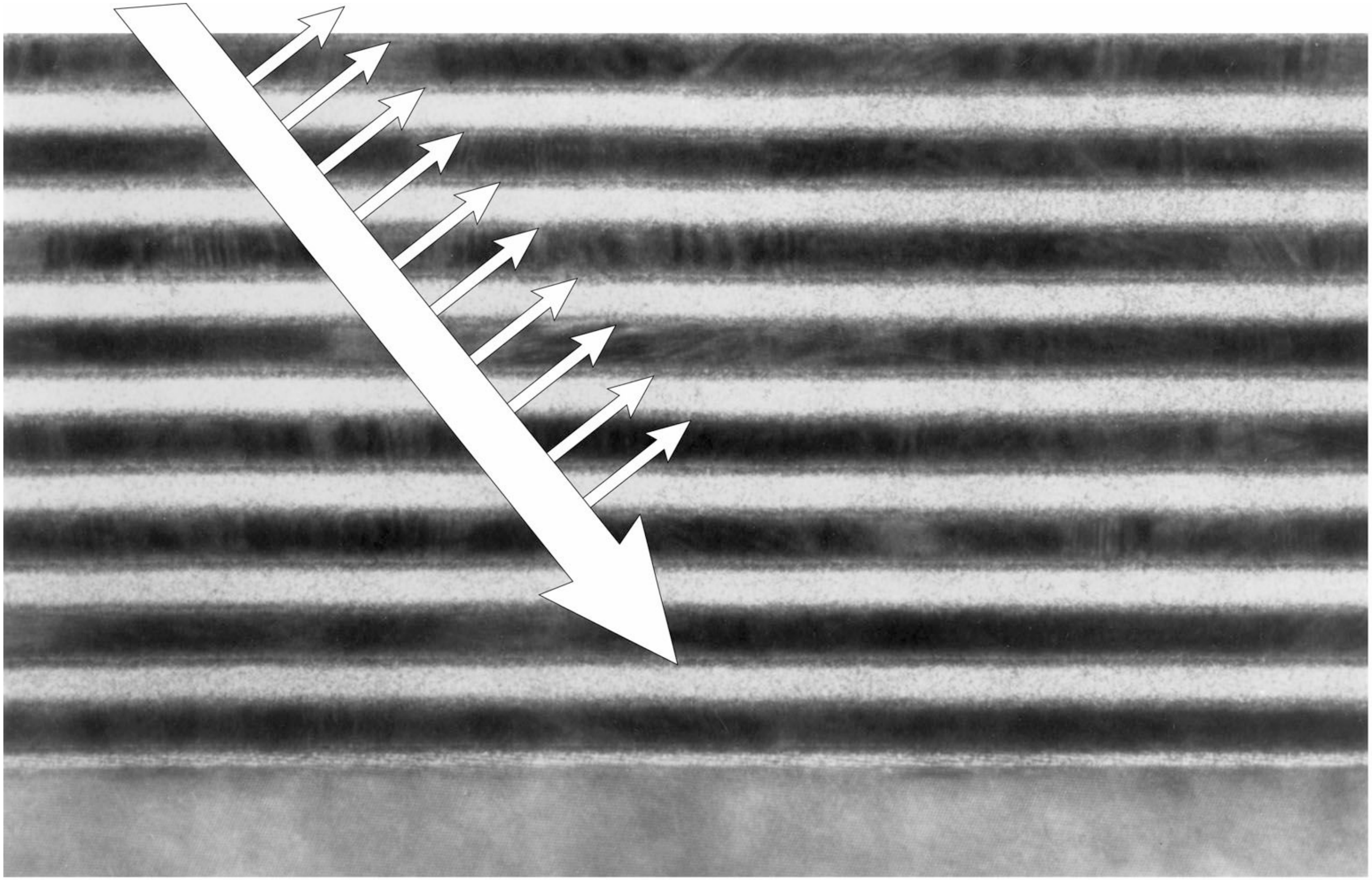

(T. Nguyen, CXRO/LBNL)

Ch04_F01_Feb2007.ai

Scattering of radiation by a sinusoidal density distribution (atoms or electrons)

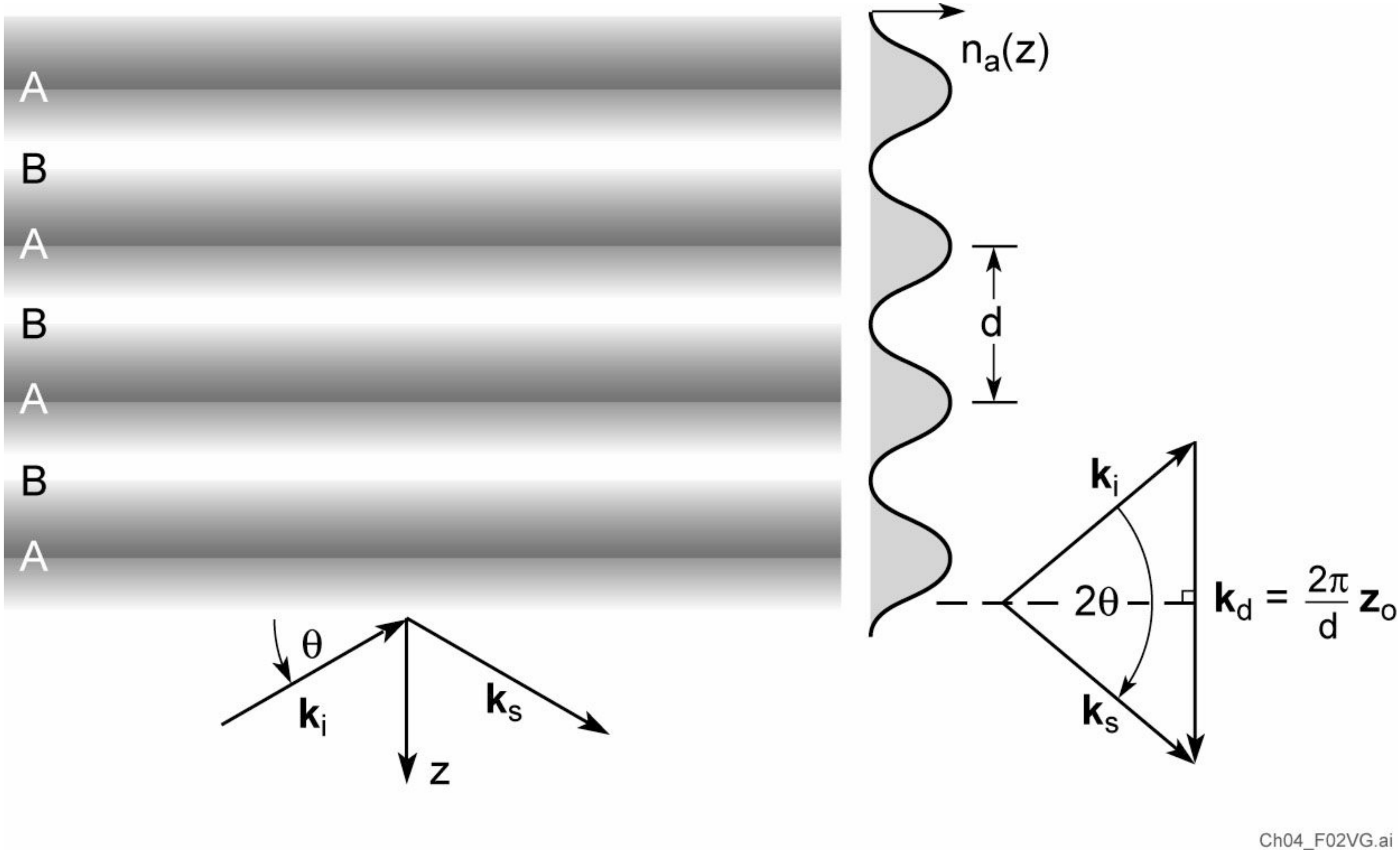

Scattering from density variations

In the long wavelength limit ($\lambda >> a_0$)

$$\mathbf{J}^0(\mathbf{r}, t) = -ef^0(\omega)n_a(\mathbf{r}, t)\mathbf{v}(\mathbf{r}, t) \tag{4.1}$$

$$\mathbf{J}_{\text{scatt}}e^{-i(\omega_s t-\mathbf{k}_s\cdot\mathbf{r})} = -ef^0(\omega_i)n_a e^{-i(\omega_d t-\mathbf{k}_d\cdot\mathbf{r})}\frac{-e\mathbf{E}_i}{-i\omega_i m}e^{-i(\omega_i t-\mathbf{k}_i\cdot\mathbf{r})} \tag{4.2}$$

$$\mathbf{J}_s = \frac{ie^2 n_a f^0(\omega_i)}{\omega_i m}\mathbf{E}_i \tag{4.3}$$

$$\omega_s = \omega_i + \omega_d \tag{4.4a}$$

$$\mathbf{k}_s = \mathbf{k}_i + \mathbf{k}_d \tag{4.4b}$$

$$\boxed{\hbar\omega_s = \hbar\omega_i + \hbar\omega_d} \tag{4.5a}$$

$$\boxed{\hbar\mathbf{k}_s = \hbar\mathbf{k}_i + \hbar\mathbf{k}_d} \tag{4.5b}$$

$$\sin\theta = \frac{k_d/2}{k_i}$$

or

$$\lambda = 2d\sin\theta \tag{4.6a}$$

$$\boxed{m\lambda = 2d\sin\theta} \tag{4.6b}$$

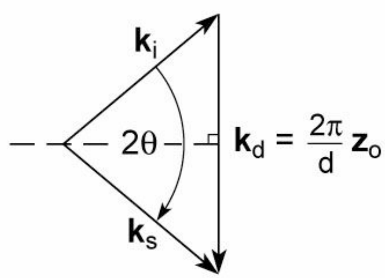

Ch04_Eqs1_6VG.ai

Multilayer mirrors satisfy the Bragg condition

$$m\lambda = 2d \sin\theta$$

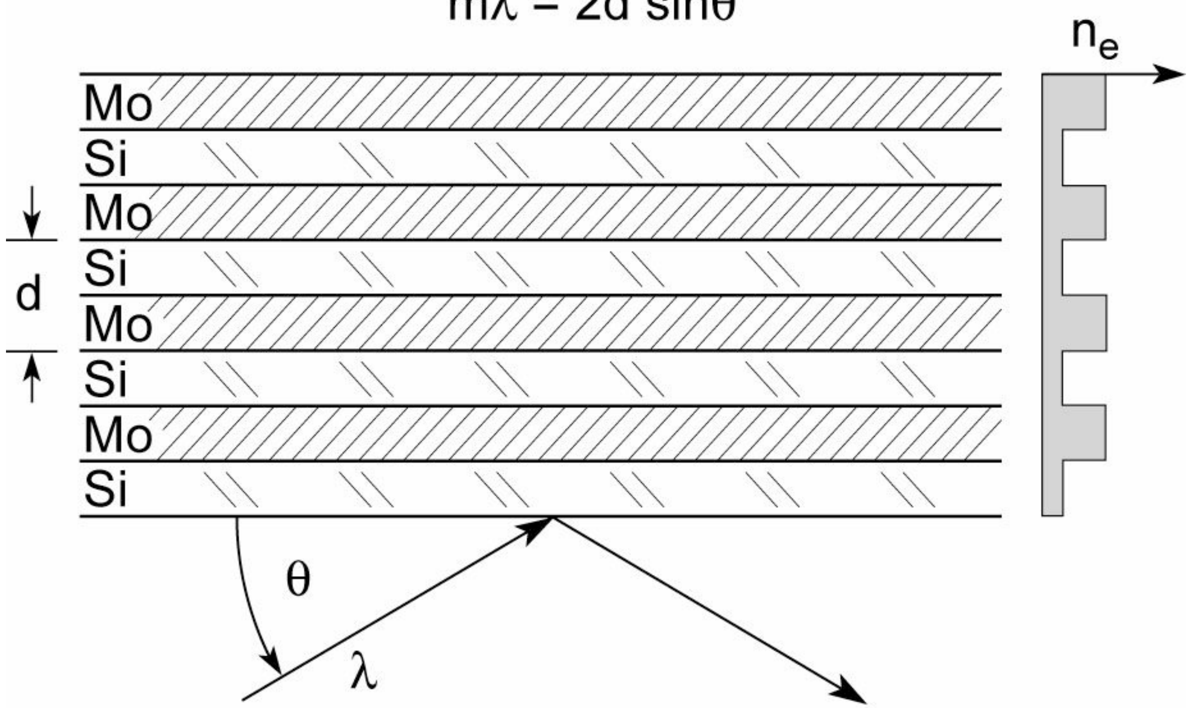

For normal incidence, $\theta = \pi/2$, first order ($m = 1$) reflection

$$\lambda = 2d$$

$$d = \lambda/2$$

if the two layers are approximately equal

$$\Delta t \simeq \lambda/4$$

a quarter-wave plate coating.

Ch04_MltlyrMirBragg1.ai

An angular scan of a multilayer mirror performs a Fourier-transform of the density profile

$$m\lambda = 2d \sin\theta$$

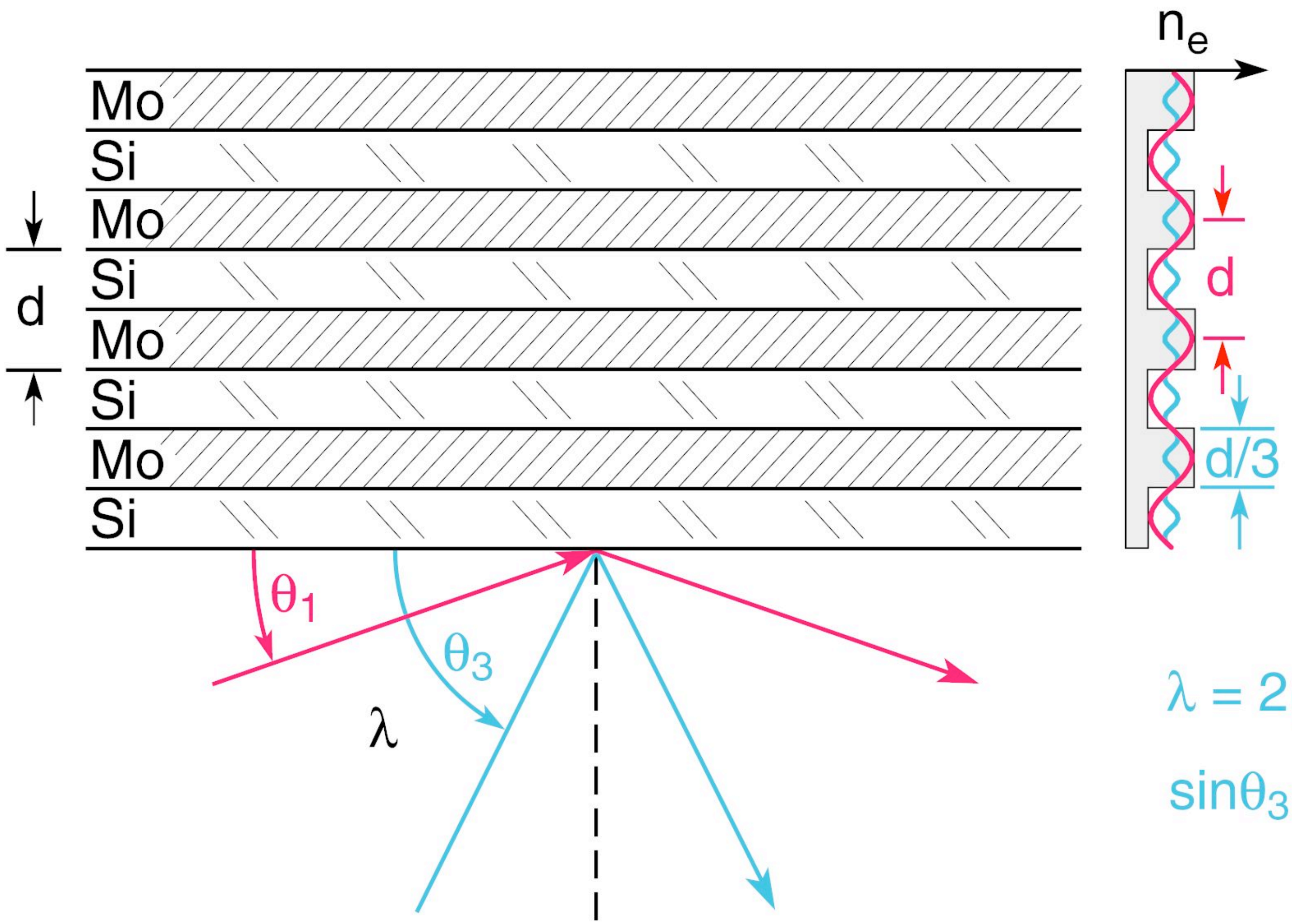

$$\lambda = 2\left(\frac{d}{3}\right)\sin\theta_3$$

$$\sin\theta_3 = 3\sin\theta_1$$

Multilayer mirrors satisfy the Bragg condition

$$m\lambda = 2d\sin\theta \left(1 - \frac{4\bar{\delta}d^2}{m^2\lambda^2}\right)$$

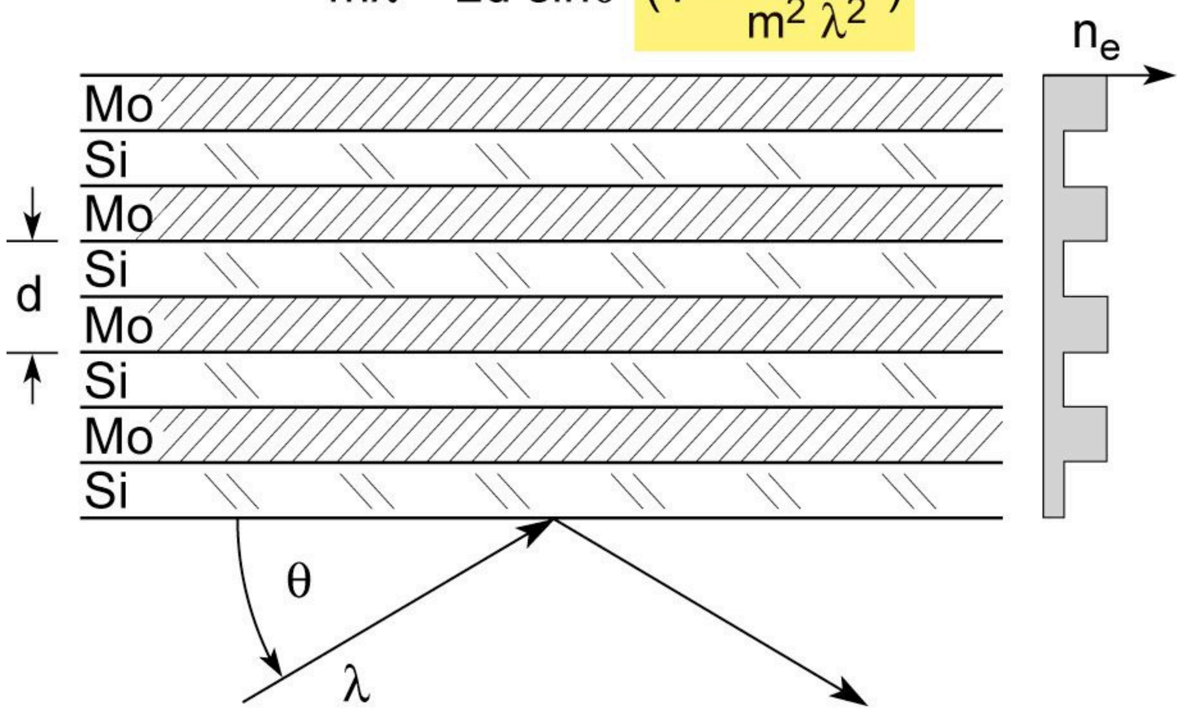

For normal incidence, $\theta = \pi/2$, first order ($m = 1$) reflection

$$\lambda = 2d$$

$$d = \lambda/2$$

if the two layers are approximately equal

$$\Delta t \simeq \lambda/4$$

a quarter-wave plate coating.

Ch04_MltlyrMirBragg2.ai

High reflectivity multilayer coatings require

- Refractive index contrast at the interfaces
- Minimal absorption in the low-Z material
- Thin high-Z layer where possible $\Gamma \equiv \Delta\tau_H / (\Delta\tau_H + \Delta\tau_L)$
- Interfaces which are chemically stable with time
- Minimal interdiffusion at the interfaces
- Minimal interfacial roughness (no crystallite formation within the layers, no shadowing in the coating process, surface mobility)
- Thermal stability during illumination
- Chemically stable vacuum interface(e.g., $Si0_2$ or capping layer)
- Uniform coating thickness

Computed reflectivity of a W/C x-ray multilayer mirror

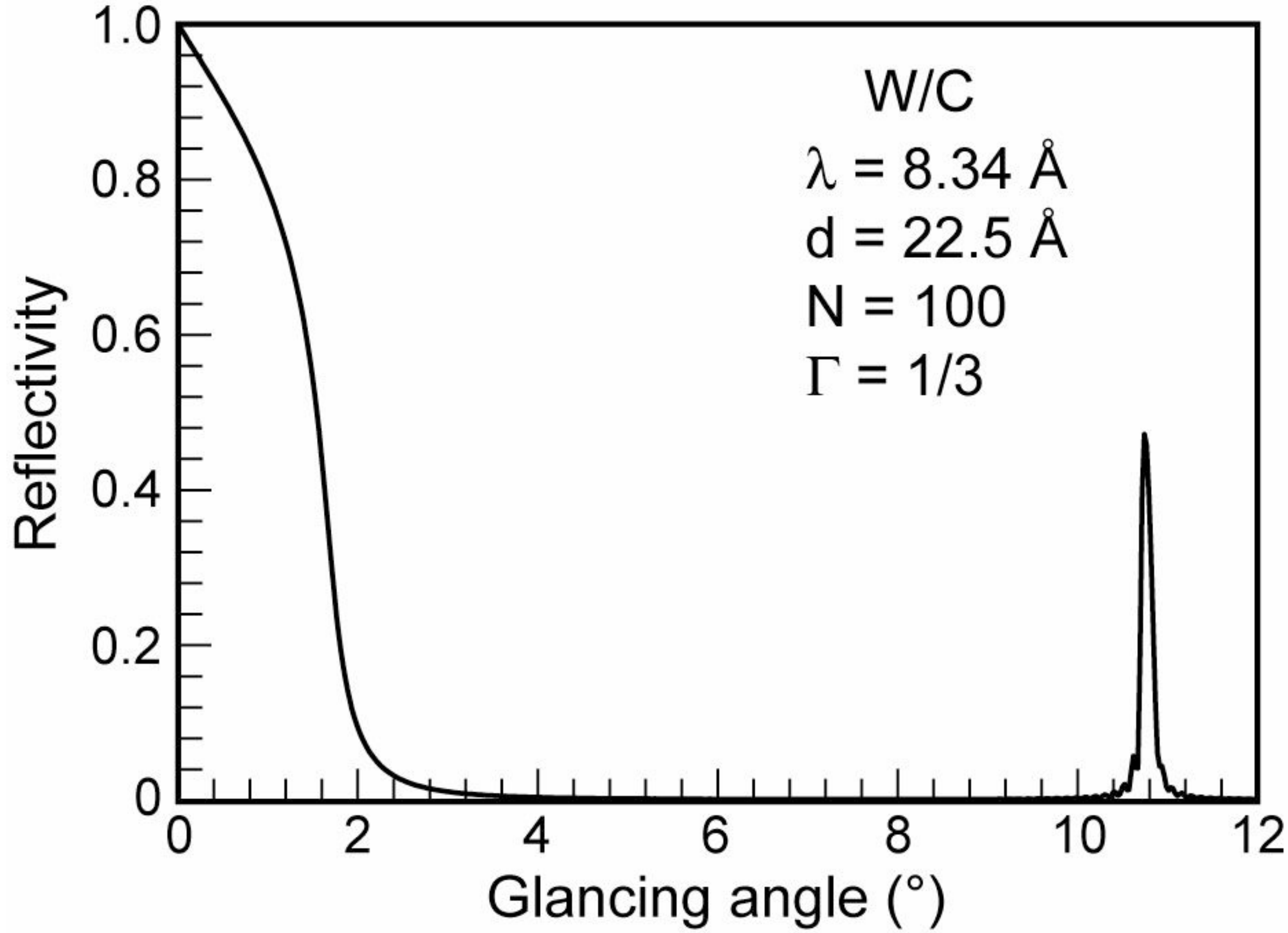

(Courtesy of J. Underwood and D. Solina)

Ch04_ComputdReflec.ai

High order reflections from a multilayer coating

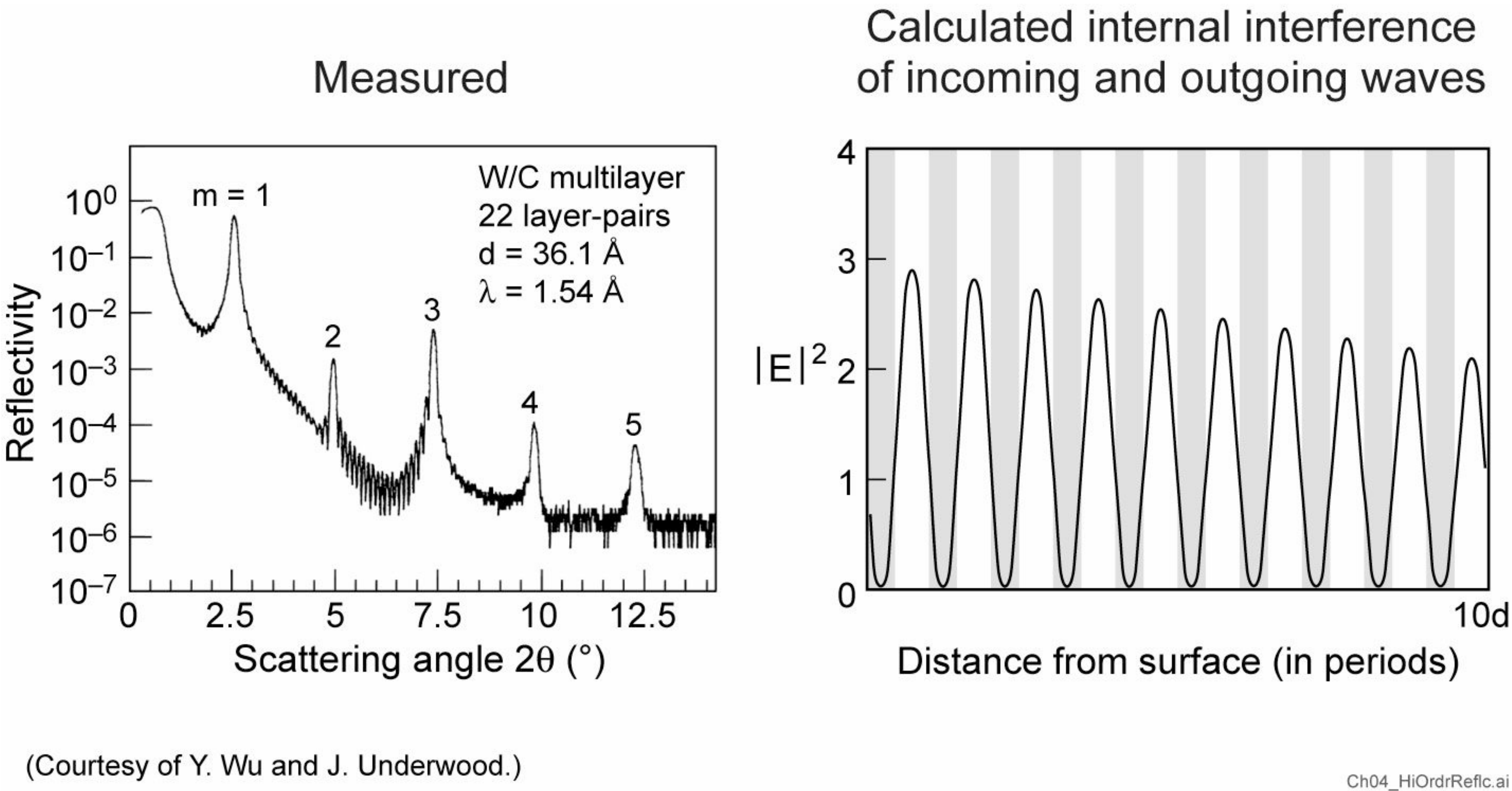

Multilayer interface mirrors computational model

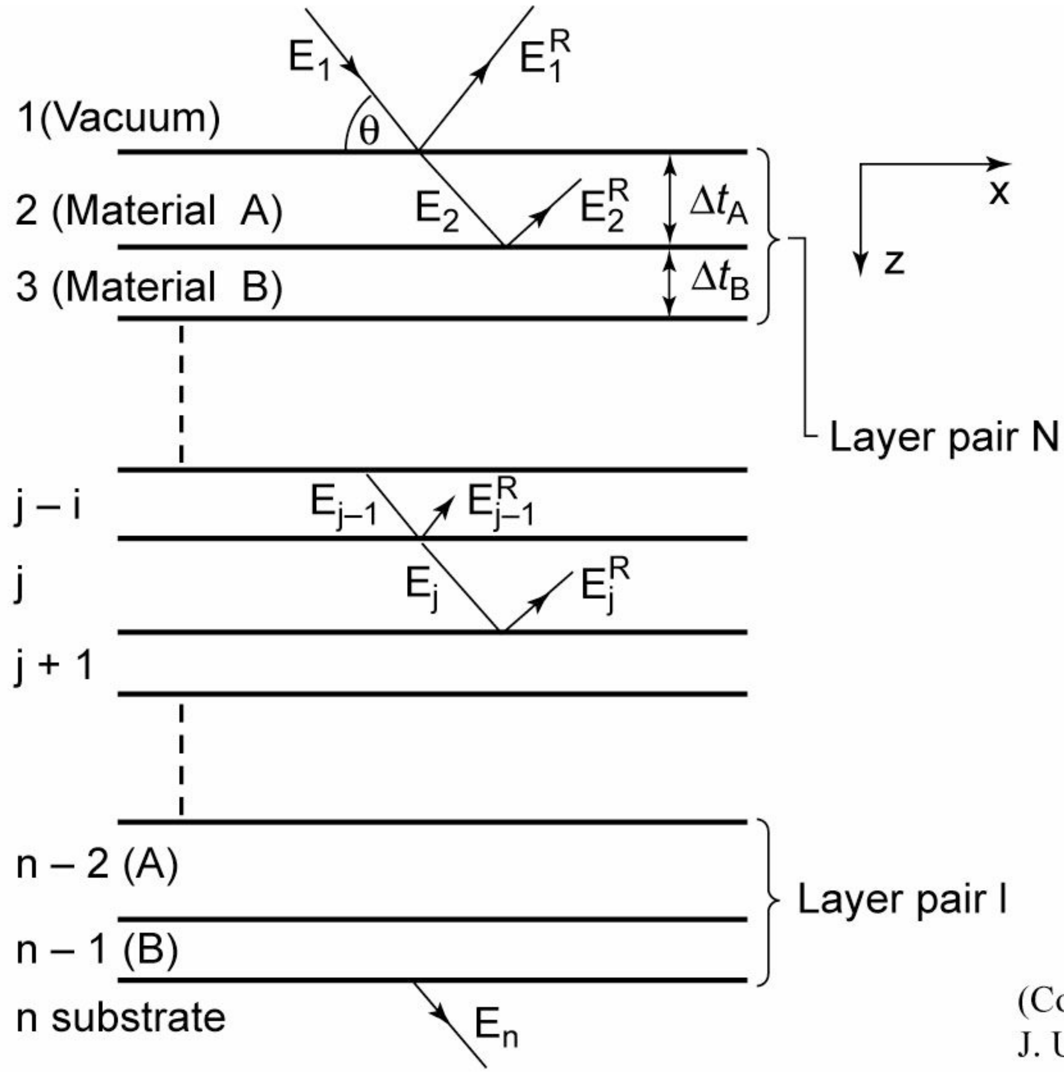

(Courtesy of J. Underwood)

With refractive index n:

www.cxro.LBL.gov

Ch04_MultlyrIntrfMir.ai

Atomic scattering factors for Silicon (Z = 14)

σ_a(barns/atom) = μ(cm^2/g) × 46.64
E(keV)μ(cm^2/g) = f_2^0 × 1498.22

Silicon (Si)
Z = 14
Atomic weight = 28.086

Energy (eV)	f_1^0	f_2^0	μ(cm^2/g)
30	3.799	3.734E–01	1.865E+04
70	2.448	5.701E–01	1.220E+04
100	–5.657	4.580E+00	6.862E+04
300	12.00	6.439E+00	3.216E+04
700	13.31	1.951E+00	4.175E+03
1000	13.00	1.070E+00	1.602E+03
3000	14.23	1.961E+00	9.792E+02
7000	14.33	4.240E–01	9.075E+01
10000	14.28	2.135E–01	3.199E+01
30000	14.02	2.285E–02	1.141E+00

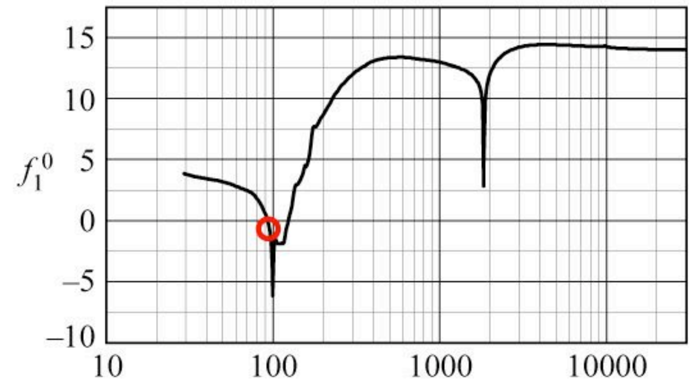

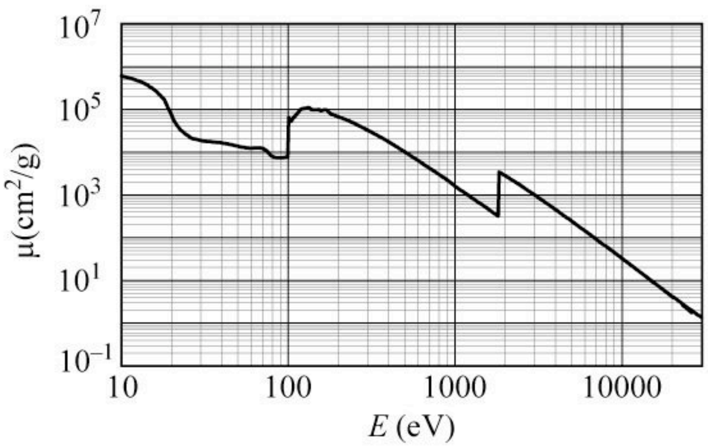

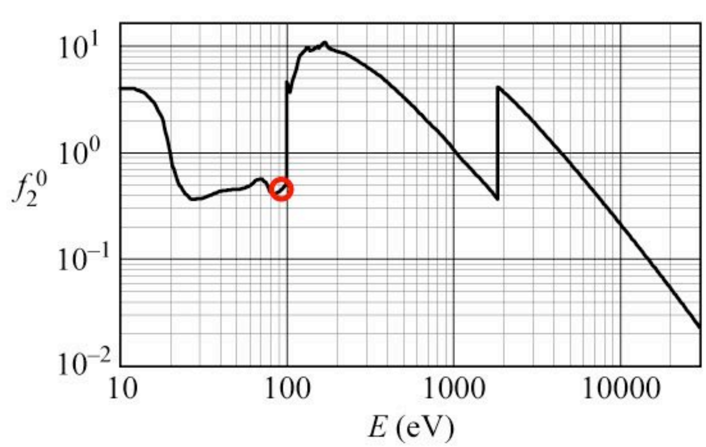

Edge Energies: K 1838.9 eV
L_1 149.7 eV
L_2 99.8 eV
L_3 99.2 eV

(Henke and Gullikson; www-cxro.LBL.gov)

Ch02ApC_Tb1F07_Sept05.ai

Atomic scattering factors for Molybdenum (Z = 42)

σ_a(barns/atom) = μ(cm^2/g) × 159.31
E(keV)μ(cm^2/g) = f_2^0 × 438.59

Molybdenum (Mo)
Z = 42
Atomic weight = 95.940

Energy (eV)	f_1^0	f_2^0	μ(cm^2/g)
30	1.071	5.292E+00	7.736E+04
70	19.38	4.732E+00	2.965E+04
100	14.02	1.124E+00	4.931E+03
300	4.609	1.568E+01	2.292E+04
700	31.41	1.819E+01	1.140E+04
1000	35.15	1.188E+01	5.210E+03
3000	35.88	1.366E+01	1.997E+03
7000	42.11	3.493E+00	2.189E+02
10000	41.67	1.881E+00	8.248E+01
30000	42.04	1.894E+00	2.769E+01

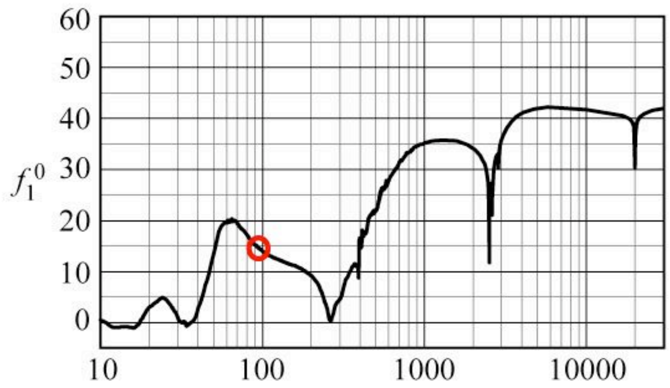

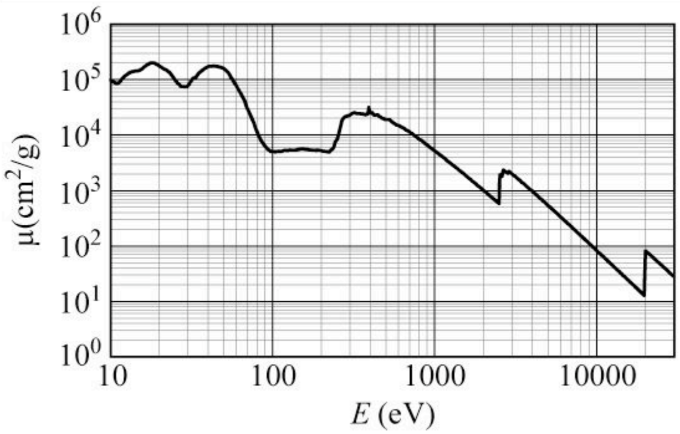

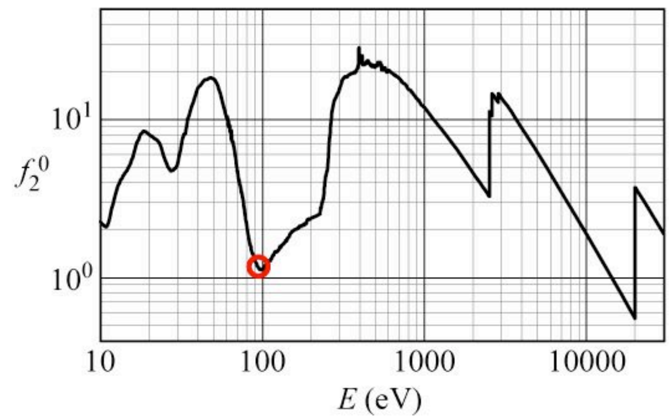

Edge Energies:

K 19999.5 eV	L_1 2865.5 eV	M_1 506.3 eV	N_1 63.2 eV
	L_2 2625.1 eV	M_2 411.6 eV	N_2 37.6 eV
	L_3 2520.2 eV	M_3 394.0 eV	N_3 35.5 eV
		M_4 231.1 eV	
		M_5 227.9 eV	

(Henke and Gullikson; www-cxro.LBL.gov)

Ch02ApC_Tb1F12_June2008.ai

Optimized reflectivity with thin "high-Z" layers

$$\Gamma = \frac{\Delta t_H}{\Delta t_H + \Delta t_L} = \frac{\Delta t_H}{d} \qquad (4.7)$$

$$\tan(\pi \Gamma_{opt}) = \pi \left[\Gamma_{opt} + \frac{\beta_L}{\beta_H - \beta_L} \right] \qquad (4.8)$$

(Vinogradov and Zeldovich, 1977)

(also see Borrmann, 1941)

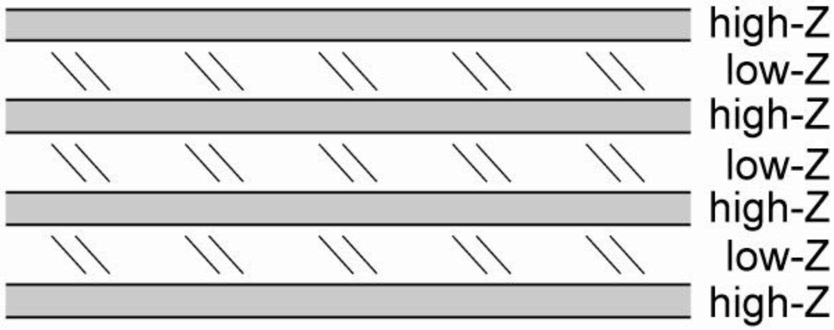

- Sharp interfaces needed for scattering
- Thin high-Z layer to minimize absorption
- Low-Z layer best as a "spacer"

Ch04_OptomizReflcty.ai

A high quality Mo/Si multilayer mirror

N = 40

d = 6.7 nm

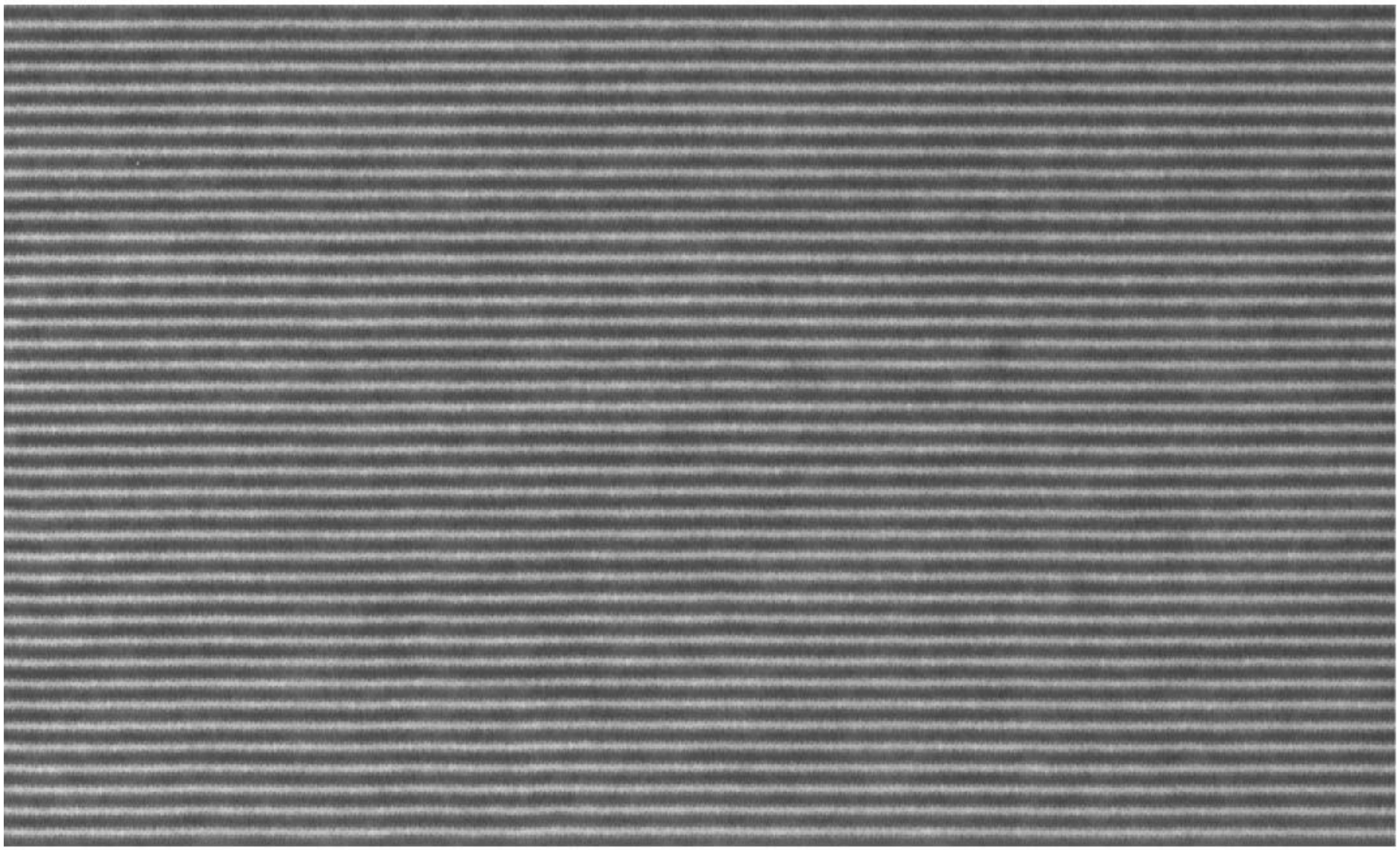

Courtesy of Saša Bajt (LLNL)

Ch04_HiQualtyMoSi.ai

Mo/Si multilayer interference coating

Molybdenum as the "scattering layer"

Silicon as the non-absorbing "spacing layer"

Actually an exaggeration, the complex refractive index of each material plays a role in the reflection process

The absorption edge Si-L_3 = 99.2 eV (12.5 nm)

Higher photon energies are absorbed in Si, lower photon energies (longer wavelengths) are not.

Typically λ = 13.4 nm or more.

Molybdenum has relatively good scattering properties in this photon energy (wavelength) region, with limited absorption.

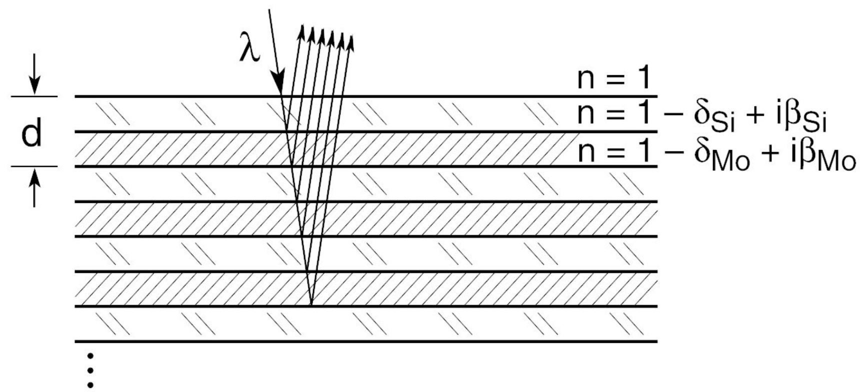

$n_{Si} = 1 - 6.6 \times 10^{-5} + i\,1.8 \times 10^{-3}$

$n_{Mo} = 0.924 + i\,7.4 \times 10^{-3}$

High reflectivity, thermally and environmentally robust multilayer coating for high throughput EUV lithography

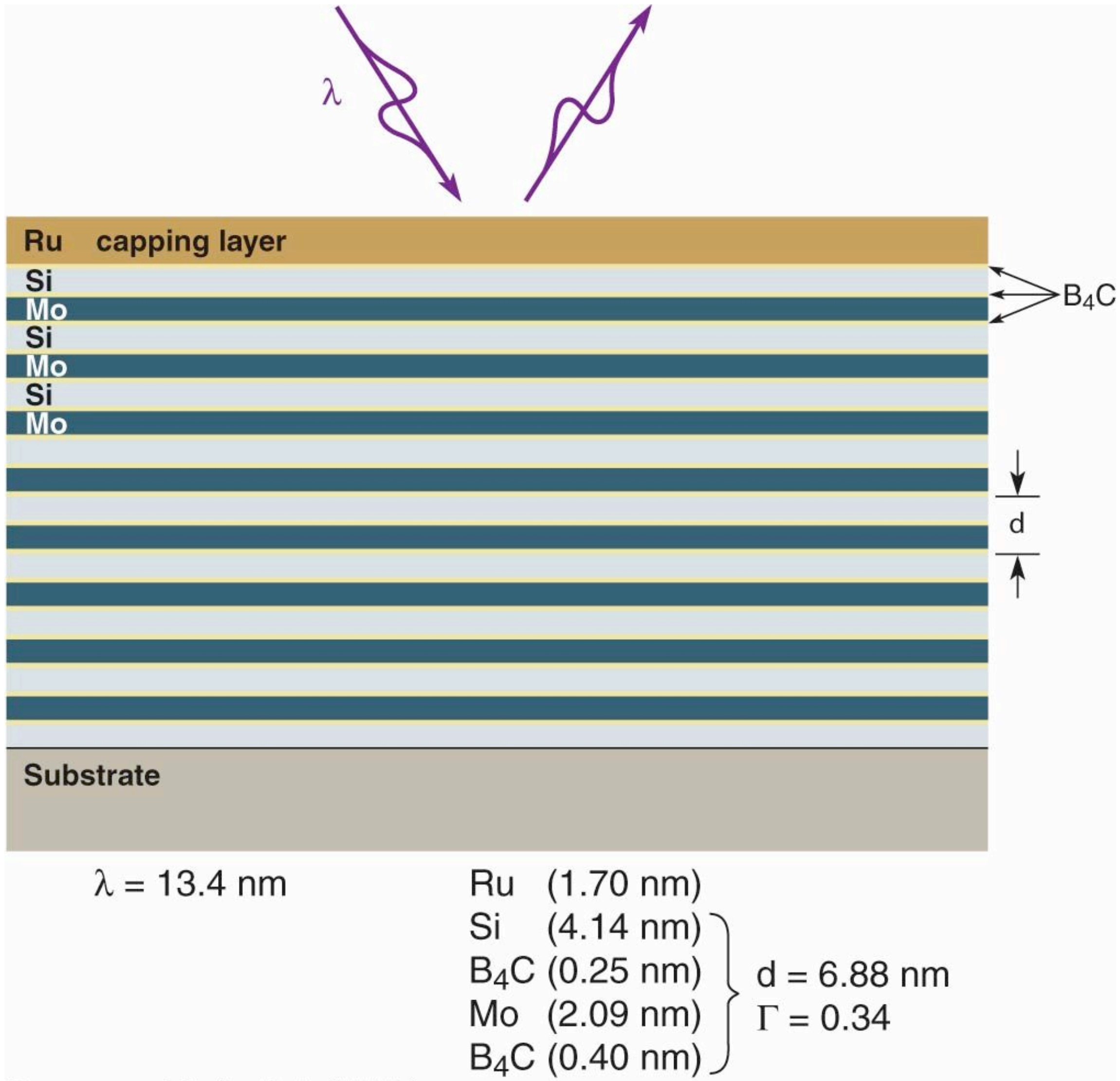

Courtesy of Saša Bajt (LLNL)

Multilayer mirrors have achieved a reflectivity of 70%

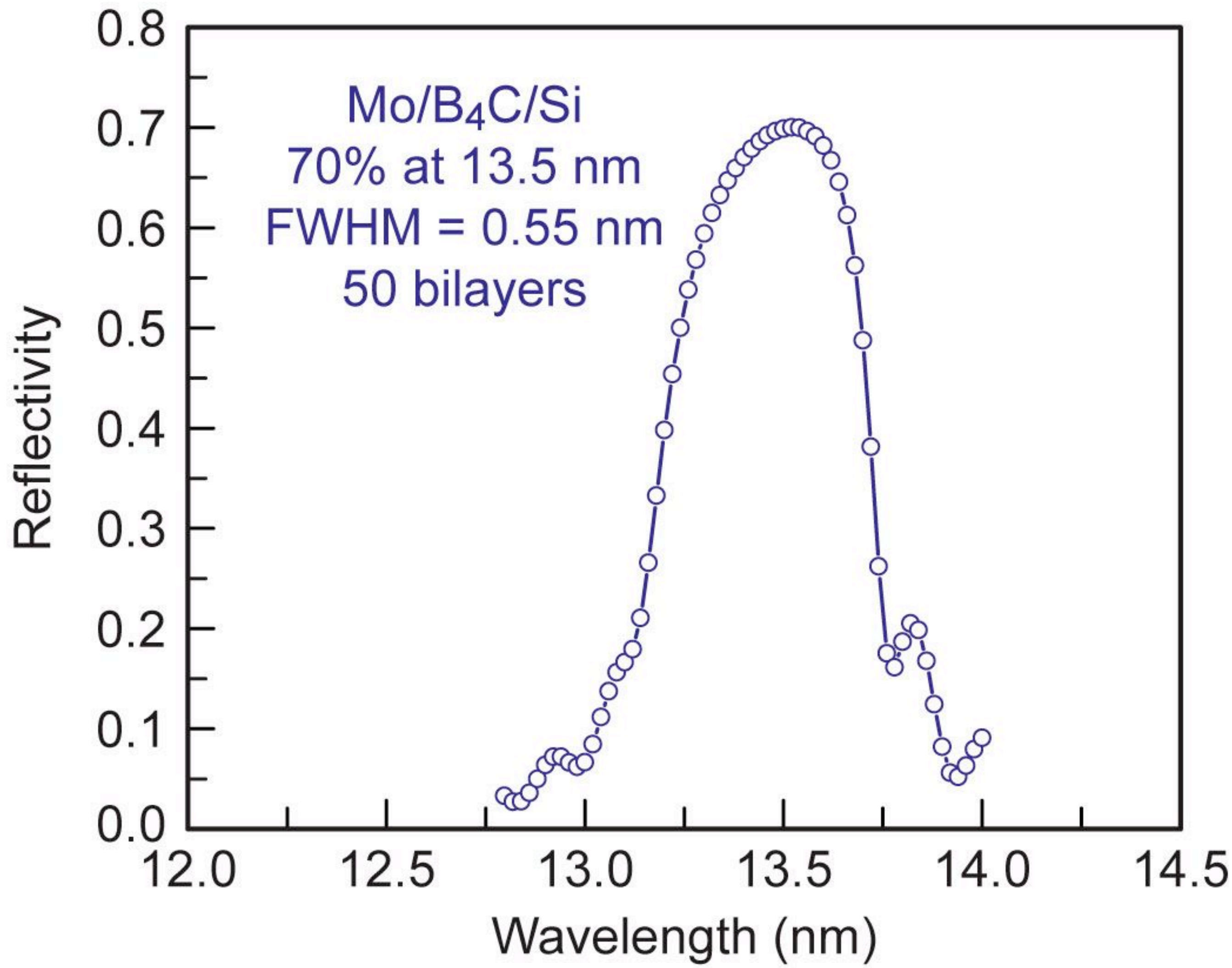

Courtesy of Saša Bajt (LLNL)

Ch04_ReflectCurv70.ai

Recent progress in multilayer mirrors

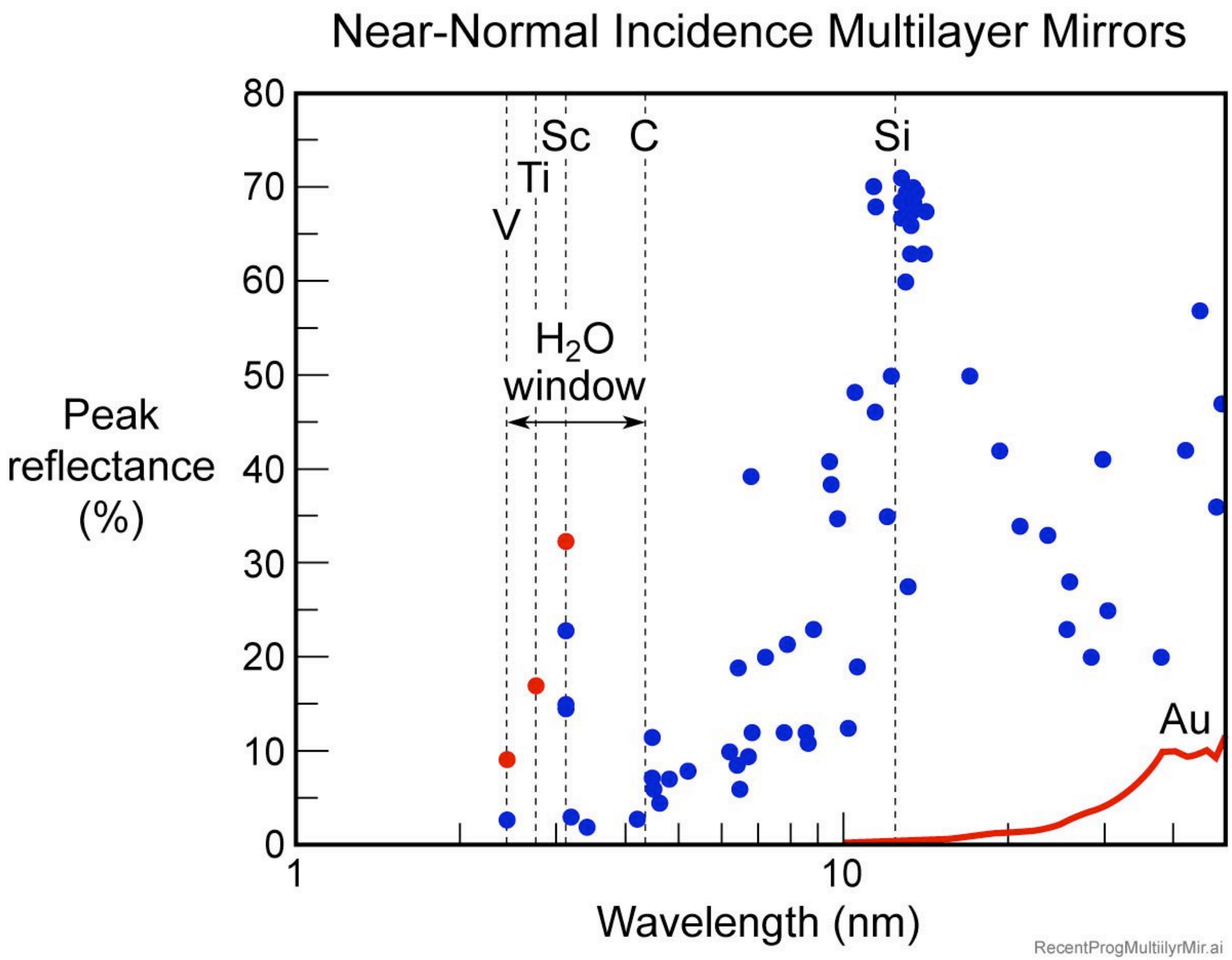

Sputtered deposition of a multilayer coating

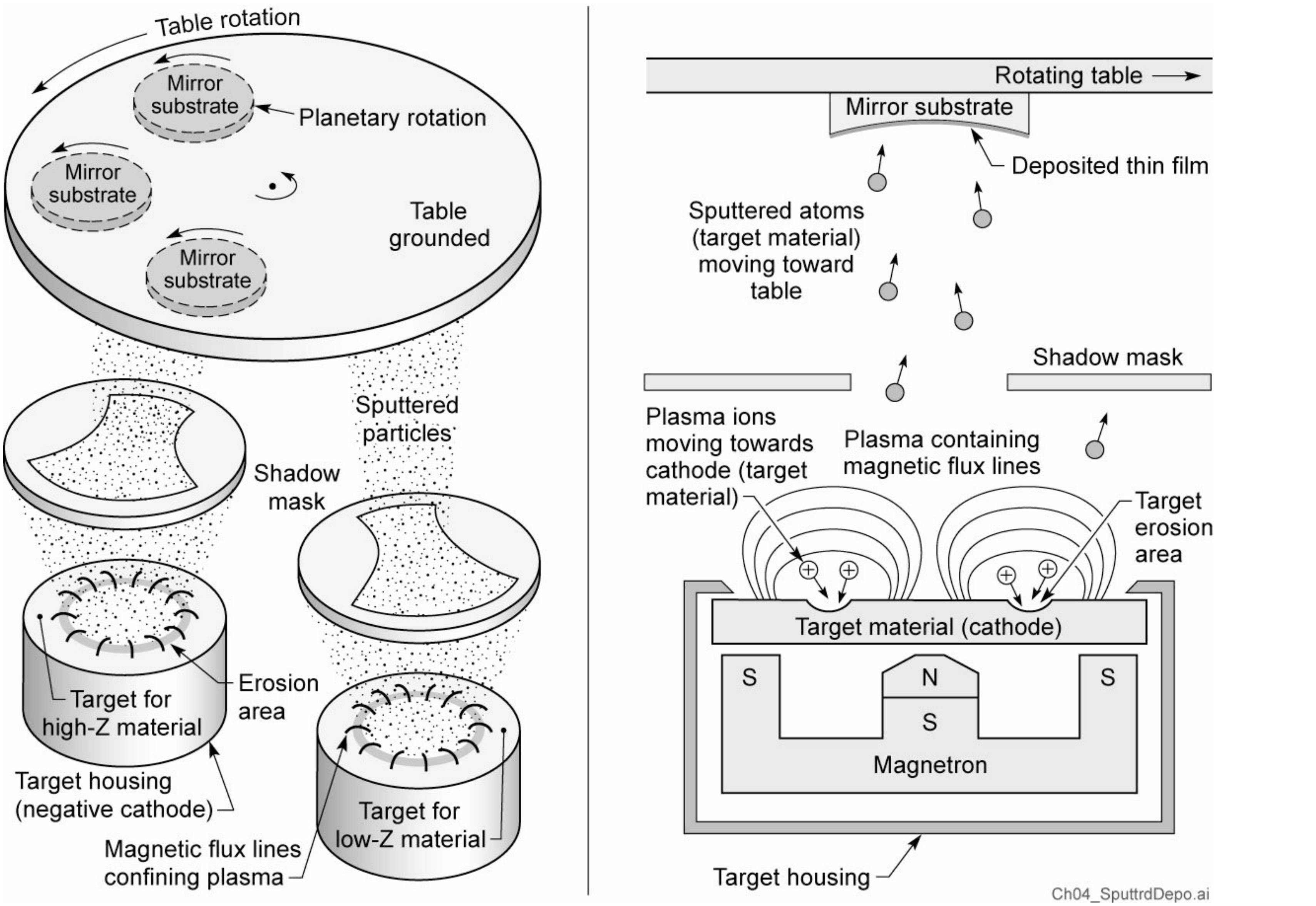

DC magnetron sputtering is used to reliably deposit multilayer coatings of predictable center wavelength and excellent uniformity

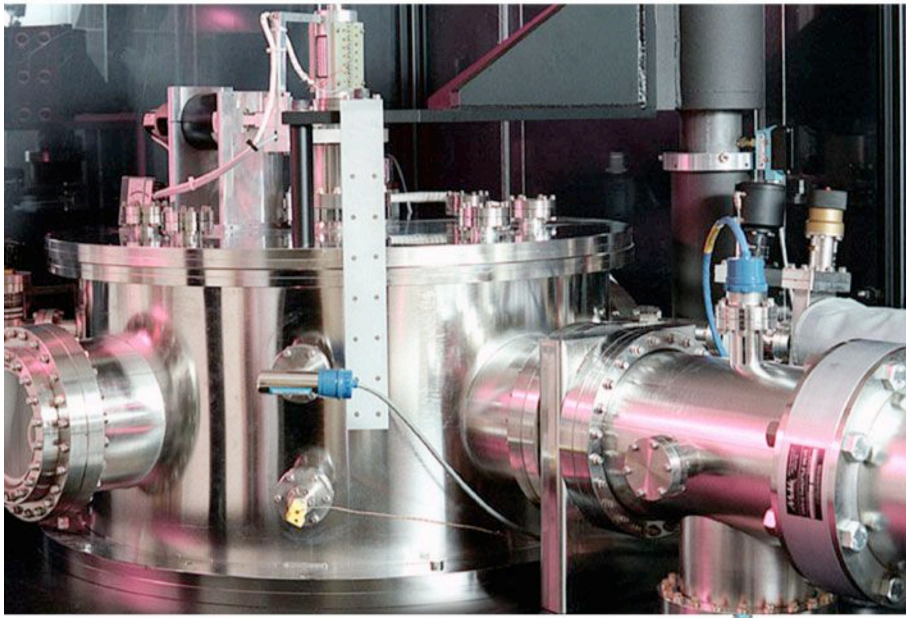

Substrates mounted on a rotating platter are swept across each sputter source sequentially to form the multilayer. Modulating the platter velocity provides precision control of radial thickness distribution and absolute film thickness. The substrate is also spun fast about its own axis for azimuthal uniformity.

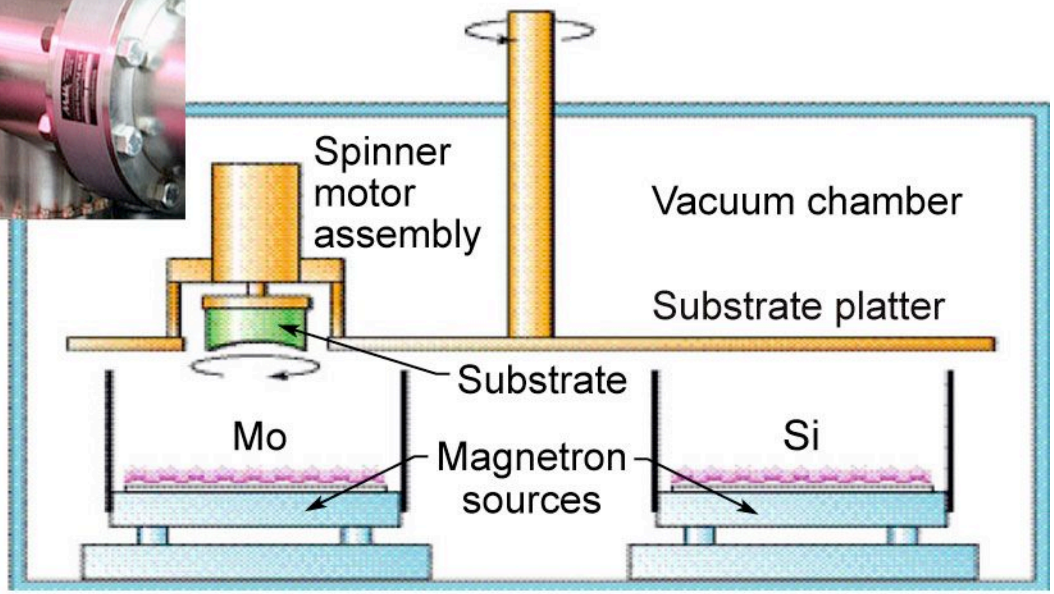

(Courtesy of Jim Folta, LLNL)

Ch04_DCmagntrn.ai

Buried, trace amounts of iron in a defective silicon solar cell

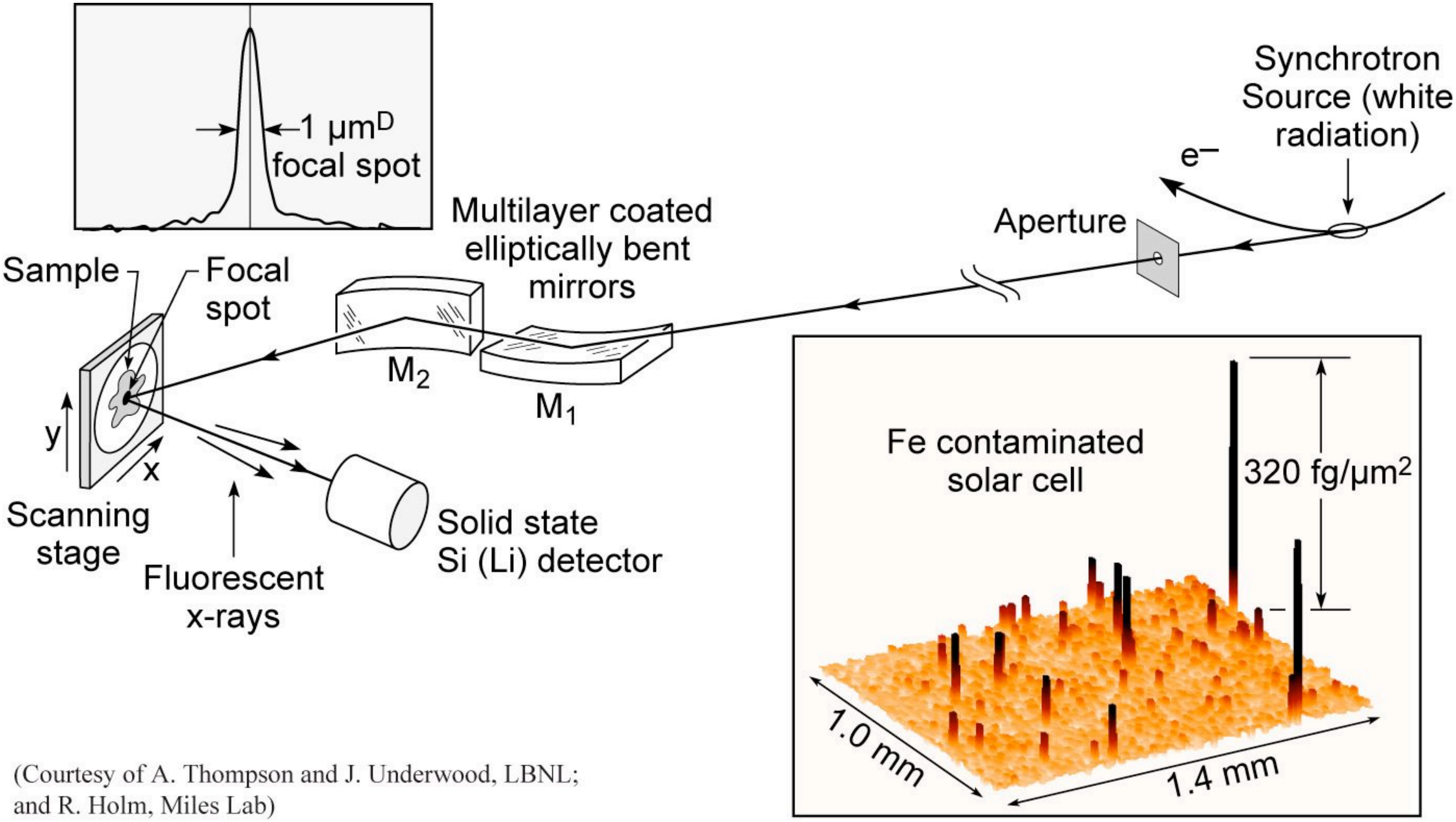

(Courtesy of A. Thompson and J. Underwood, LBNL; and R. Holm, Miles Lab)

Ch04_F14VG.ai

Microprobe analysis of contaminated soil

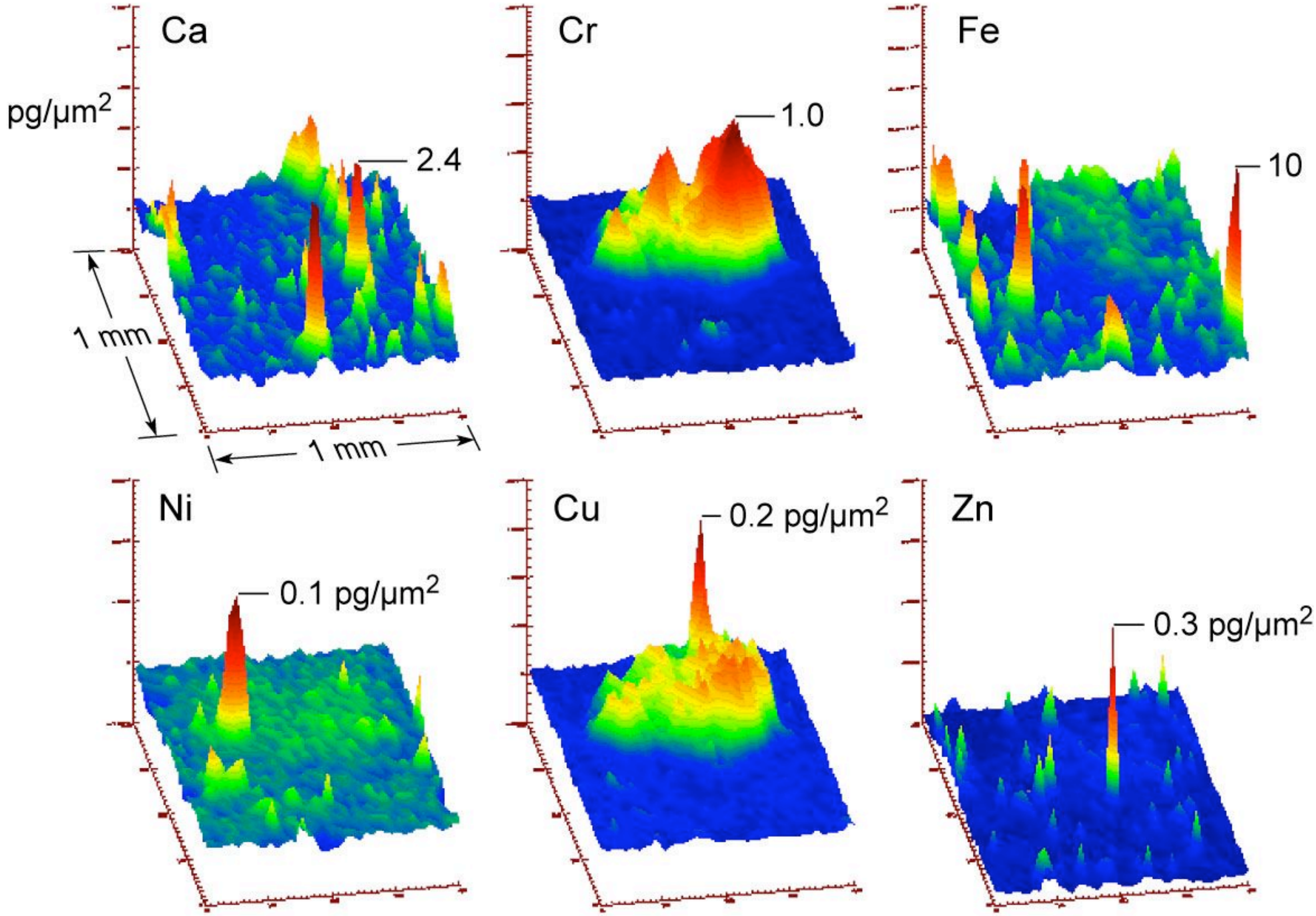

(Courtesy of T. Tokunaga; and A. Thompson, LBNL)

Ch04_F15VG.ai

Polarization studies of magnetic materials

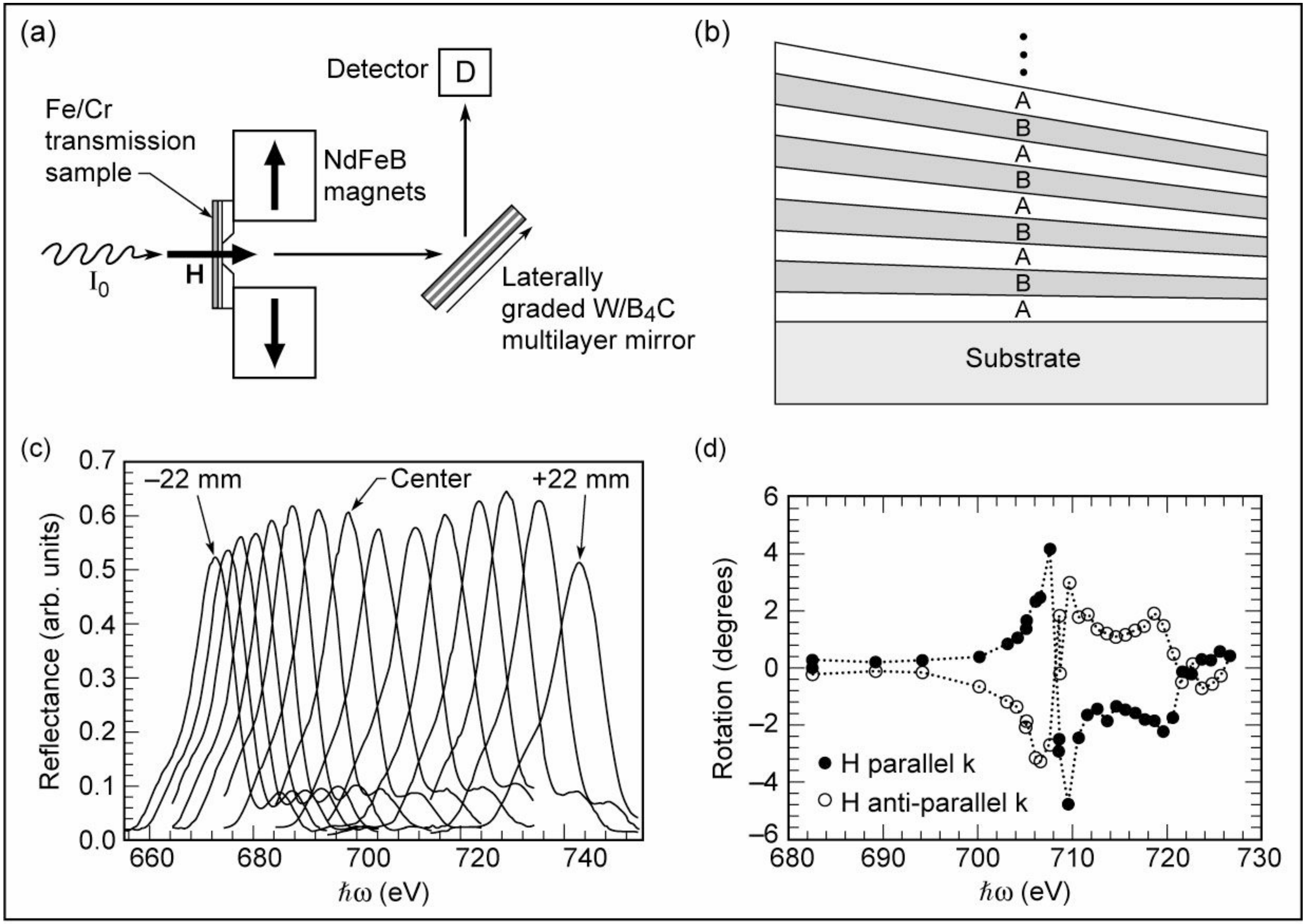

(Courtesy of J. Kortright and M. Rice, LBNL; and R. Carr, Stanford)

Ch04_PolarizStudies.ai

Photoemission microscopy for surface science and characterization

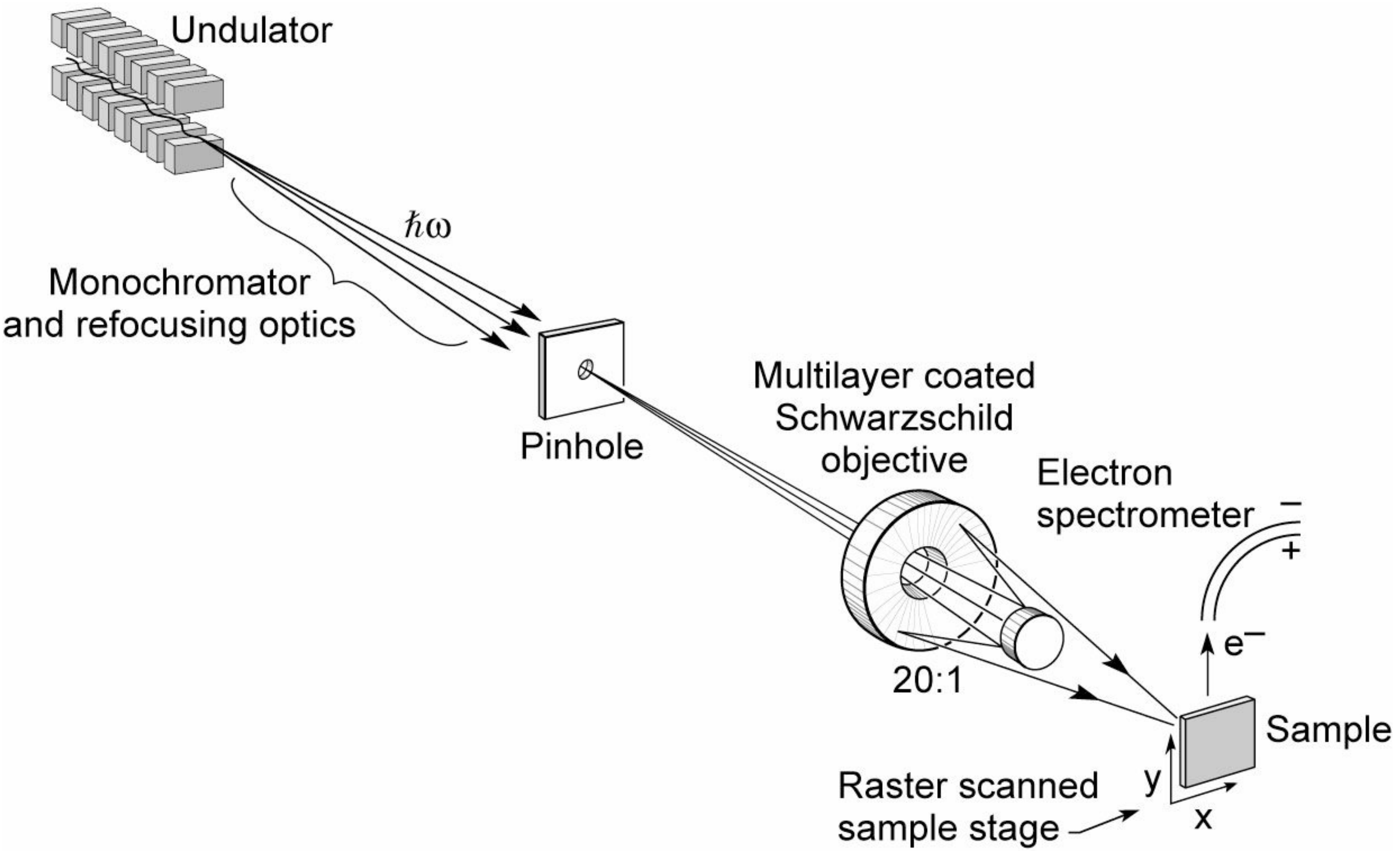

(Courtesy of F. Cerrina, Univ. Wisconsin, Madison and J. Underwood, CXRO, LBNL, Berkeley)

Ch04_PhotoemisMicro.ai

Photoemission spectroscopy reveals characteristic electron binding energies

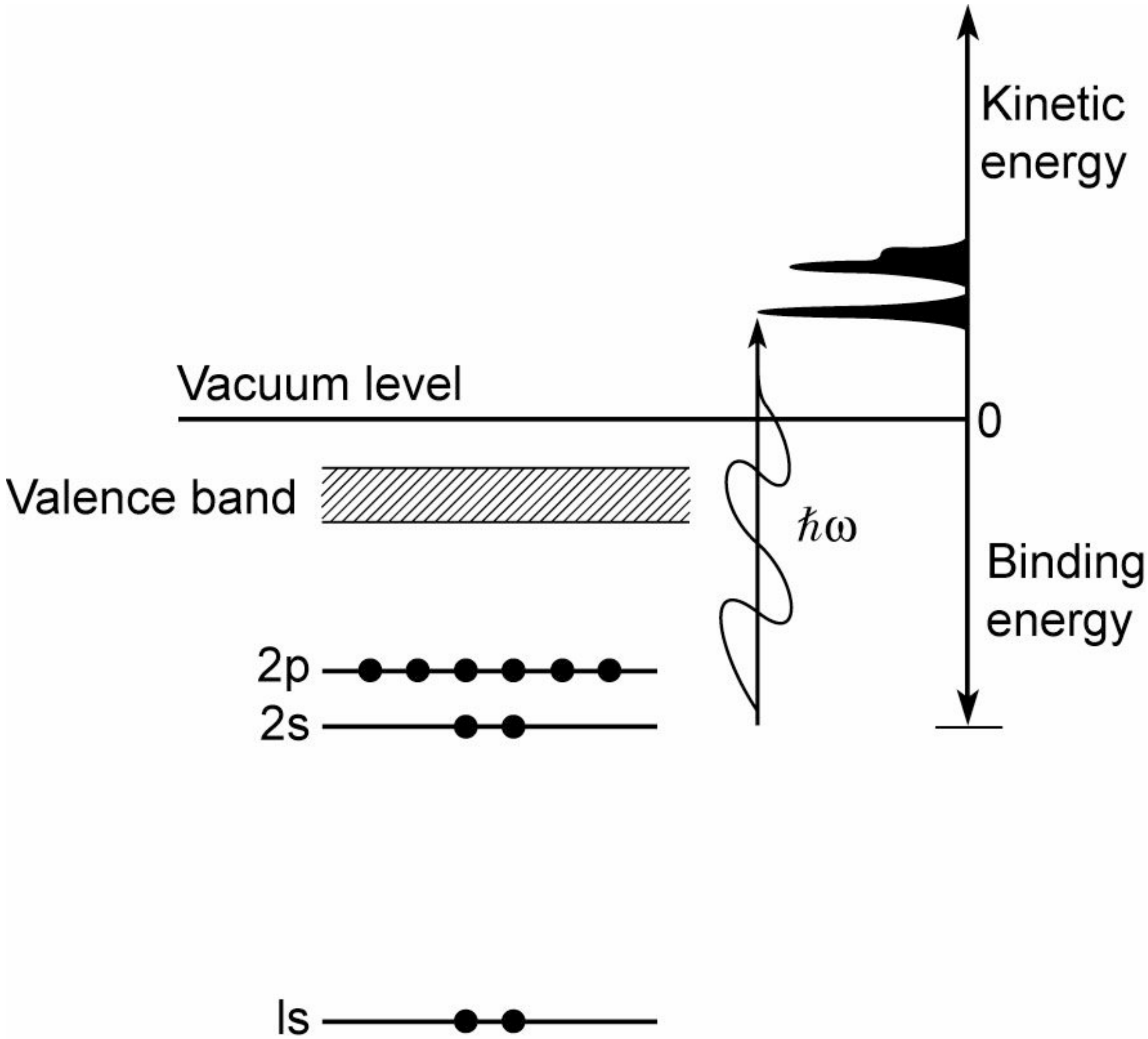

F.9.38

Ch04_PhotoemisSpectr1.ai

Photoemission spectroscopy as a tool for surface science

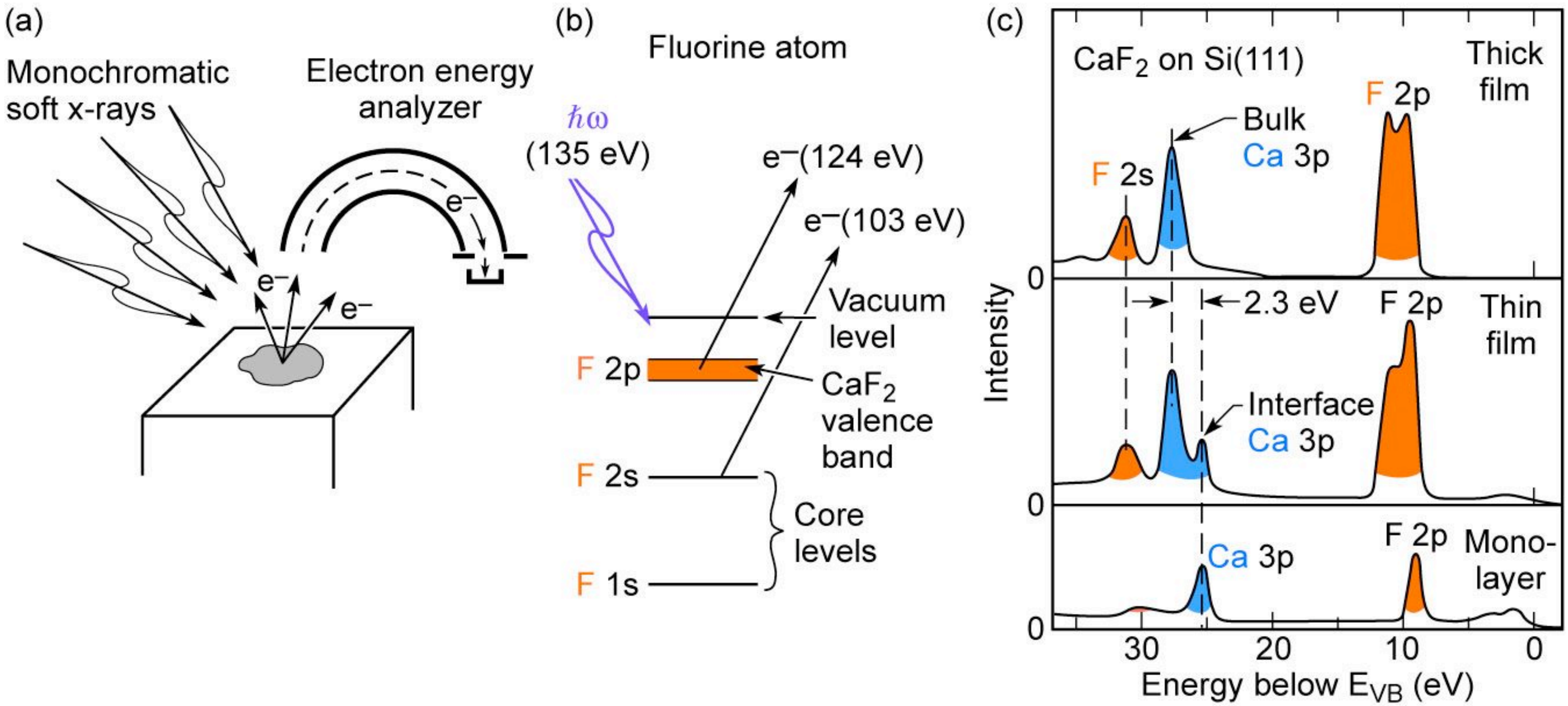

(Courtesy of M. Olmstead, Univ. Washington, Seattle)

Colorplate XIX

Ch04_PhotoemisSpectr2.ai

Observation of varied chemical states by photoemission spectromicroscopy

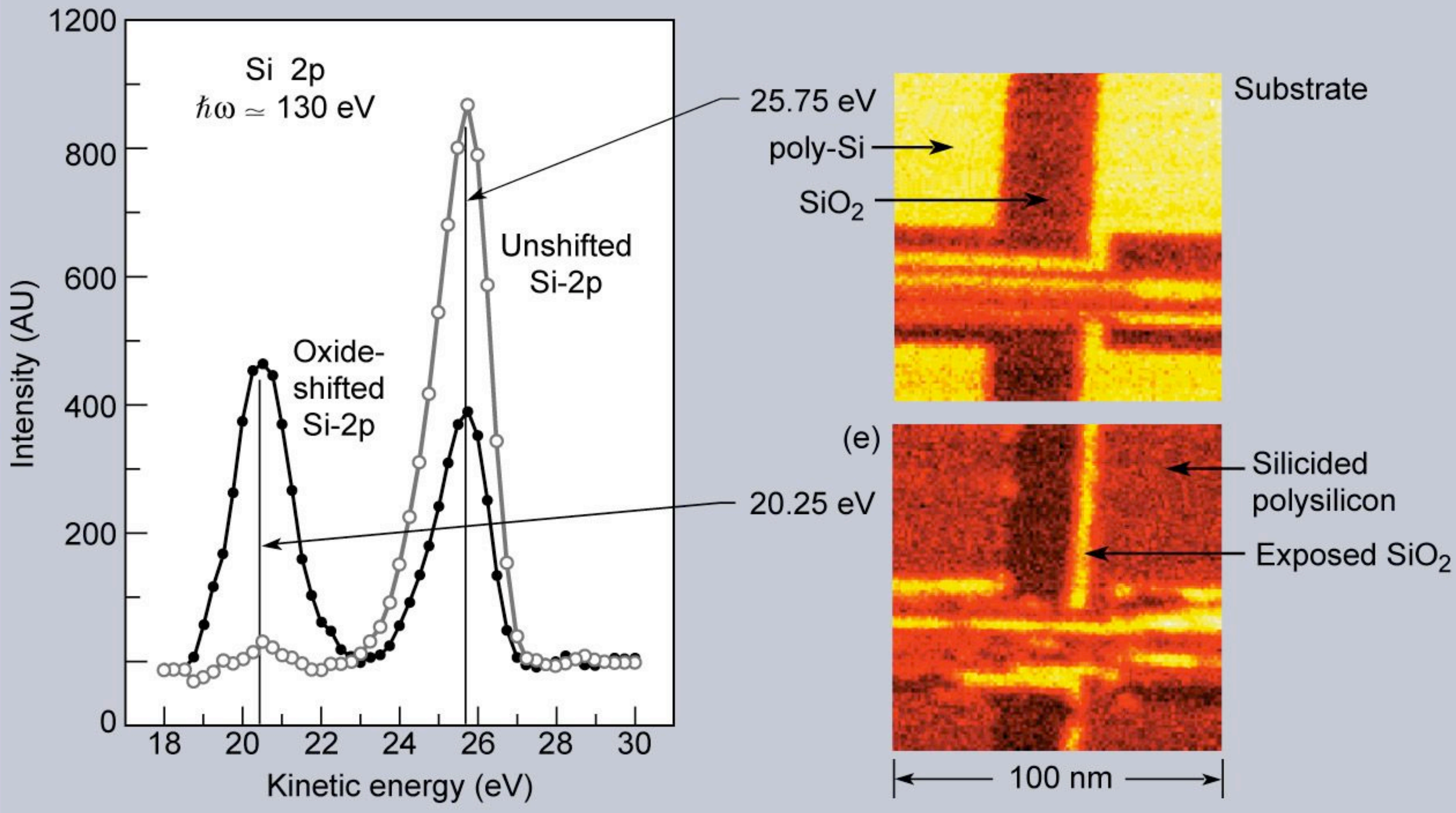

Agglomeration of $TiSi_2$ during annealing appears to have exposed SiO_2 near the edges of the poly pads

Colorplate XXII c & d

(Courtesy of S. Singh and F. Cerrina, Univ. Wisconsin, Madison)

Ch04_ObservChemSt.ai

Photoemission microscopy of a AlGaN film – “Monet”

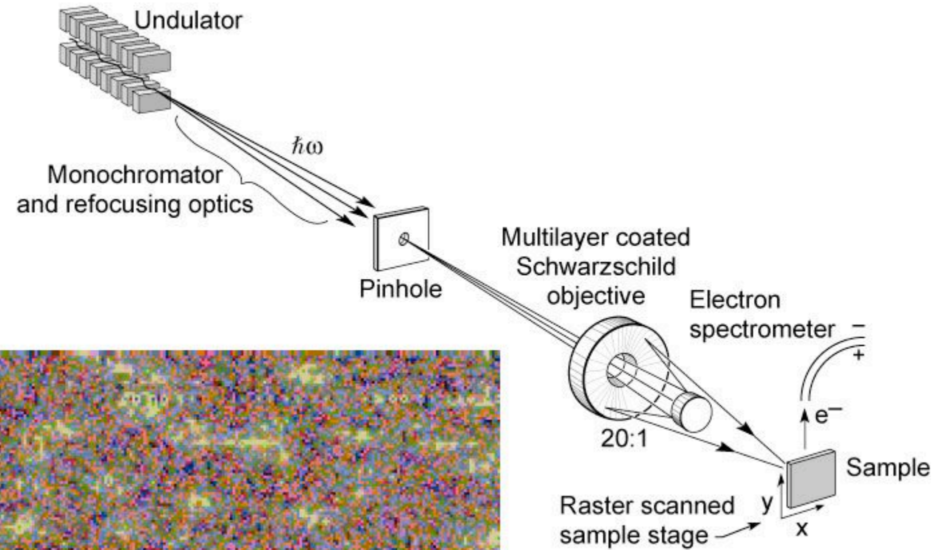

“Monet”

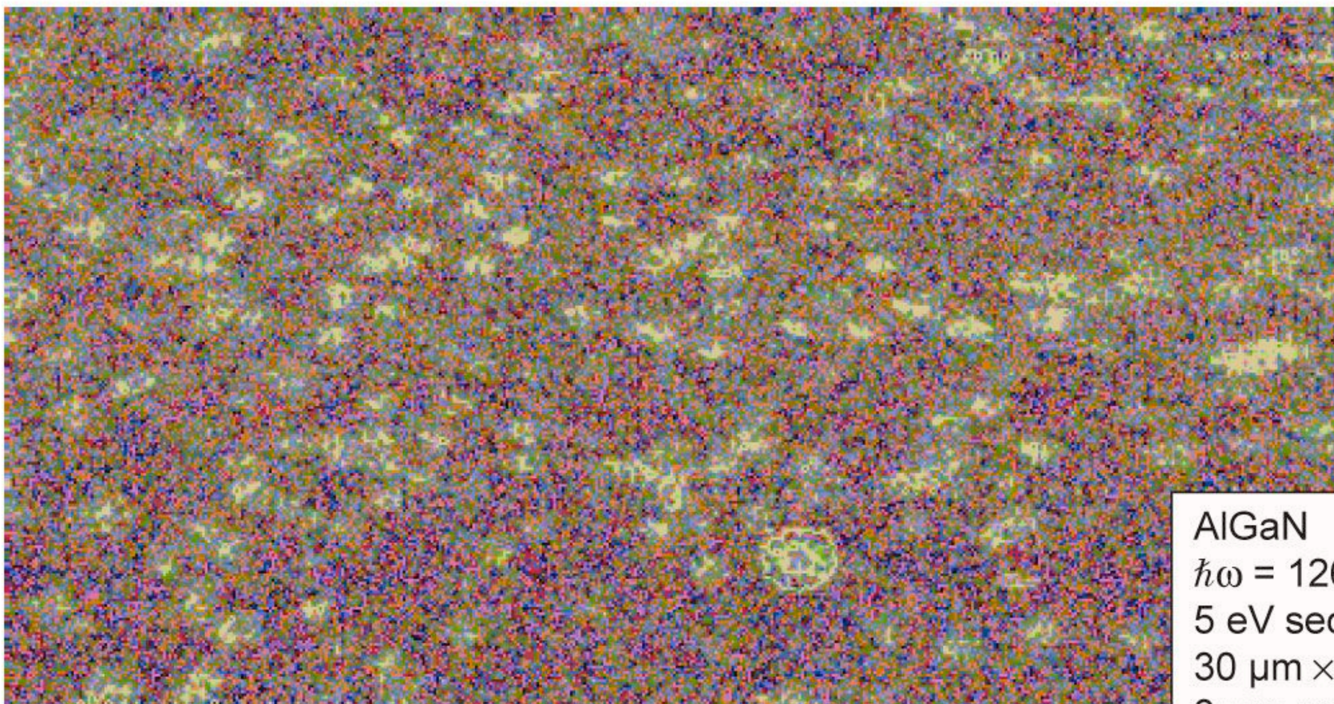

(Courtesy of G.-F. Lorusso and F. Cerrina, Univ. Wisconsin, Madison, and Advanced Light Source, Berkeley)

AlGaN
$\hbar\omega$ = 126 eV
5 eV secondary electrons
30 μm × 60 μm
3 μm grain size

Colorplate III a & c
Ch04_Photoemis_Monet.ai

High resolution x-ray diffraction under high pressure using multilayer coated focusing optics

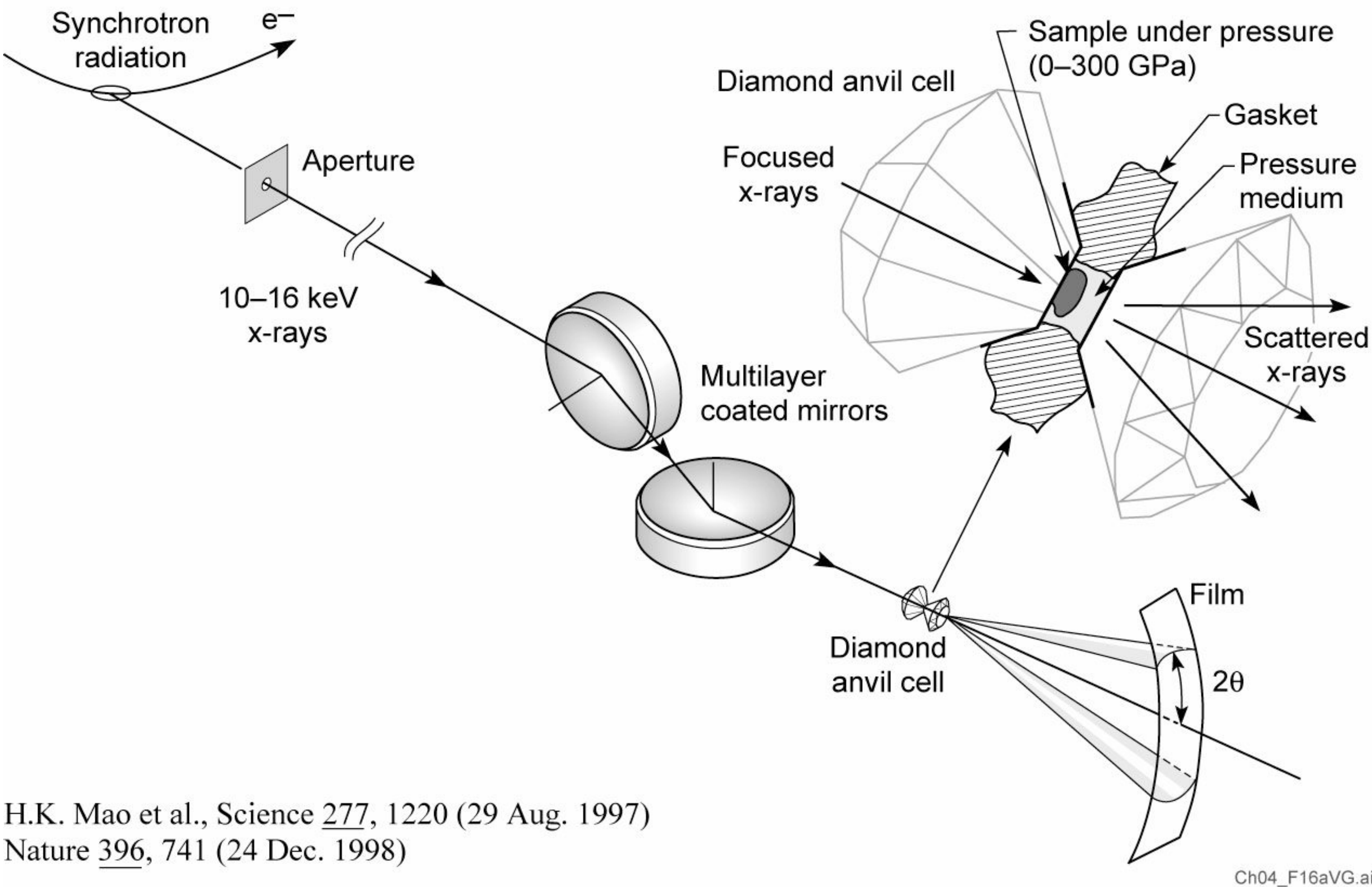

H.K. Mao et al., Science 277, 1220 (29 Aug. 1997)
Nature 396, 741 (24 Dec. 1998)

Elasticity and rheology of iron above 220 GPa and the nature of the Earth's inner core

Ho-kwang Mao*, Jinfu Shu*, Guoyin Shen†, Russell J. Hemley*, Baosheng Li‡ & Anil K. Singh§

* *Geophysical Laboratory and Center for High Presure Research, Carnegie Institution of Washington, 5251 Broad Branch Road, NW, Washington DC 20015, USA*

† *Consortium for Advanced Radiation Sources, University of Chicago, Chicago, Illinois 60637, USA*

‡ *Center for High Pressure Research, Mineral Physics Institute, State University at Stony Brook, Stony Brook, New York 11794-2100, USA*

§ *Materials Science Division, National Aerospace Laboratories, Bangalore 560017, India*

Recent numerical-modelling and seismological results have raised new questions about the dynamics[1,2] and magnetism[3,4] of the Earth's core. Knowledge of the elasticity and texture of iron[5,6] at core pressures is crucial for understanding the seismological observations, such as the low attenuation of seismic waves, the low shear-wave velocity[7,8] and the anisotropy of compressional-wave velocity[9–11]. The density and bulk modulus of hexagonal-close-packed iron have been previously measured to core pressures by static[12] and dynamic[13,14] methods. Here we study, using radial X-ray diffraction[15] and ultrasonic techniques[16], the shear modulus, single-crystal elasticity tensor, aggregate compressional- and shear-wave velocities, and orientation dependence of these velocities in iron. The inner core shear-wave velocity is lower than the aggregate shear-wave velocity of iron, suggesting the presence of low-velocity components or anelastic effects in the core. Observation of a strong lattice strain anisotropy in iron samples indicates a large (~24%) compressional-wave anisotropy under the isostress assumption, and therefore a perfect alignment of crystals[6] would not be needed to explain the seismic observations. Alternatively the strain anisotropy may indicate stress variation due to preferred slip systems.

probed the lattice strain of the sample as a function of the angle (ψ) to the diamond-cell axis[15]. At 21 pressures between 16 and 211 GPa, energy dispersive X-ray diffraction (EDXD) patterns containing (*hkl* notation) 100, 002, 101, 102, 110, 103, 112, 201 diffraction lines of hexagonal close packed (h.c.p.) iron, 111, 200, 220, 311, 222, 400, 331, 420, 422, 511 of gold, or 110, 200, 211, 220, 310, 222, 321, 400 of tungsten, were collected at 10° steps of ψ from 0° to 90°. The *d*-spacing varies linearly with $\cos^2\psi$:

$$d(hkl) = d_p(hkl)[1 + (1 - 3\cos^2\psi)Q(hkl)] \quad (3)$$

where the intercept $d_P(hkl)$ denotes the *d*-spacing under σ_P, and the slope $Q(hkl)$ is the lattice strain under the uniaxial stress condition[18,19].

In run 1, a separate gold layer was used as a standard for determination of t and shear modulus G of h.c.p. Fe. The axial stress is continuous across the interface between the gold and iron layers ($\sigma_{3Au} = \sigma_{3Fe}$; subscripts denote the Au or Fe layer), that is

$$t_{Fe} = 1.5(\sigma_3 - \sigma_{PFe}) = 1.5(\sigma_{PAu} - \sigma_{PFe}) + t_{Au} \quad (4)$$

Now, t is related to G by

$$t = 6G\langle Q\rangle \quad (5)$$

where $\langle Q\rangle$ denotes the average value of measured Q for all (hkl) (ref. 15). The hydrostatic stress components, σ_{PAu} and σ_{PFe}, were determined from the observed $d_P(hkl)$ (equation (3)) and the equations of state of Au and Fe (refs 20, 21); G_{Au} was extrapolated from low-pressure data[22,23]. The aggregate compressional-wave speed (v_P) and shear-wave speed (v_S) of h.c.p. Fe are calculated from the bulk modulus K_{Fe} and G_{Fe}. In addition (run 3), the aggregate ultrasonic

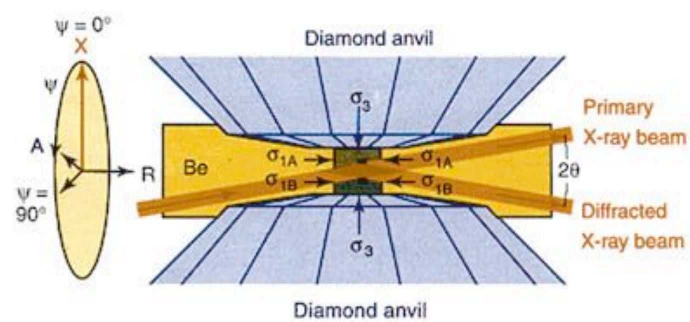

The Cassegrain telescope

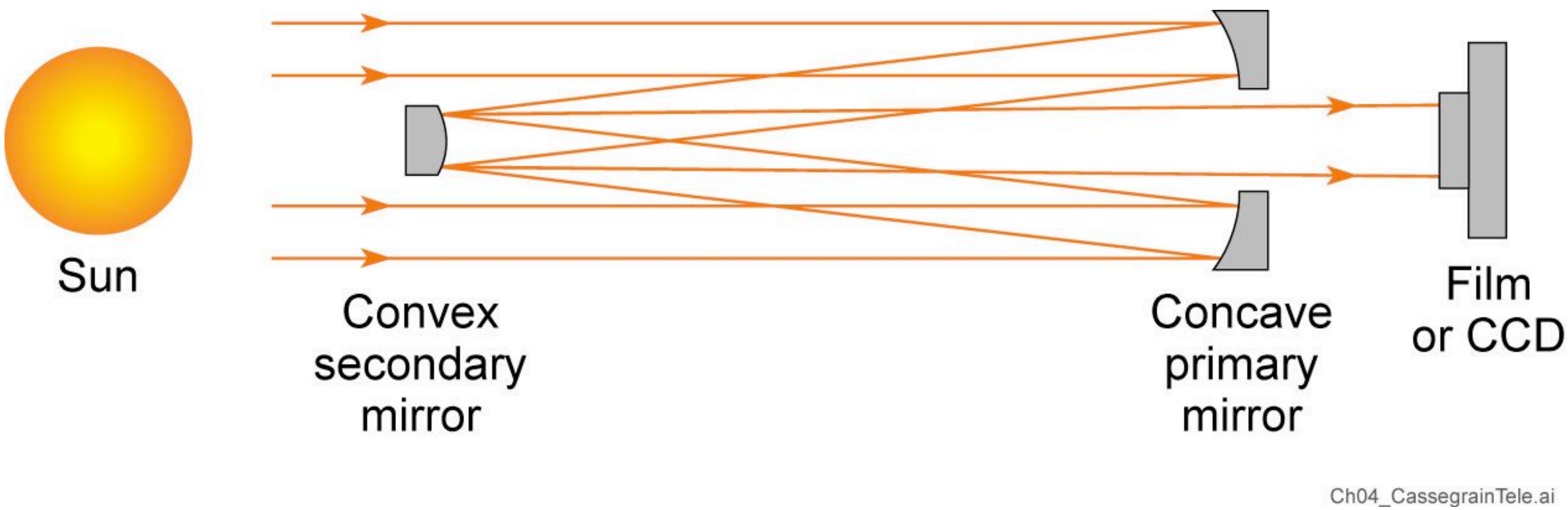

Extreme ultraviolet astronomy

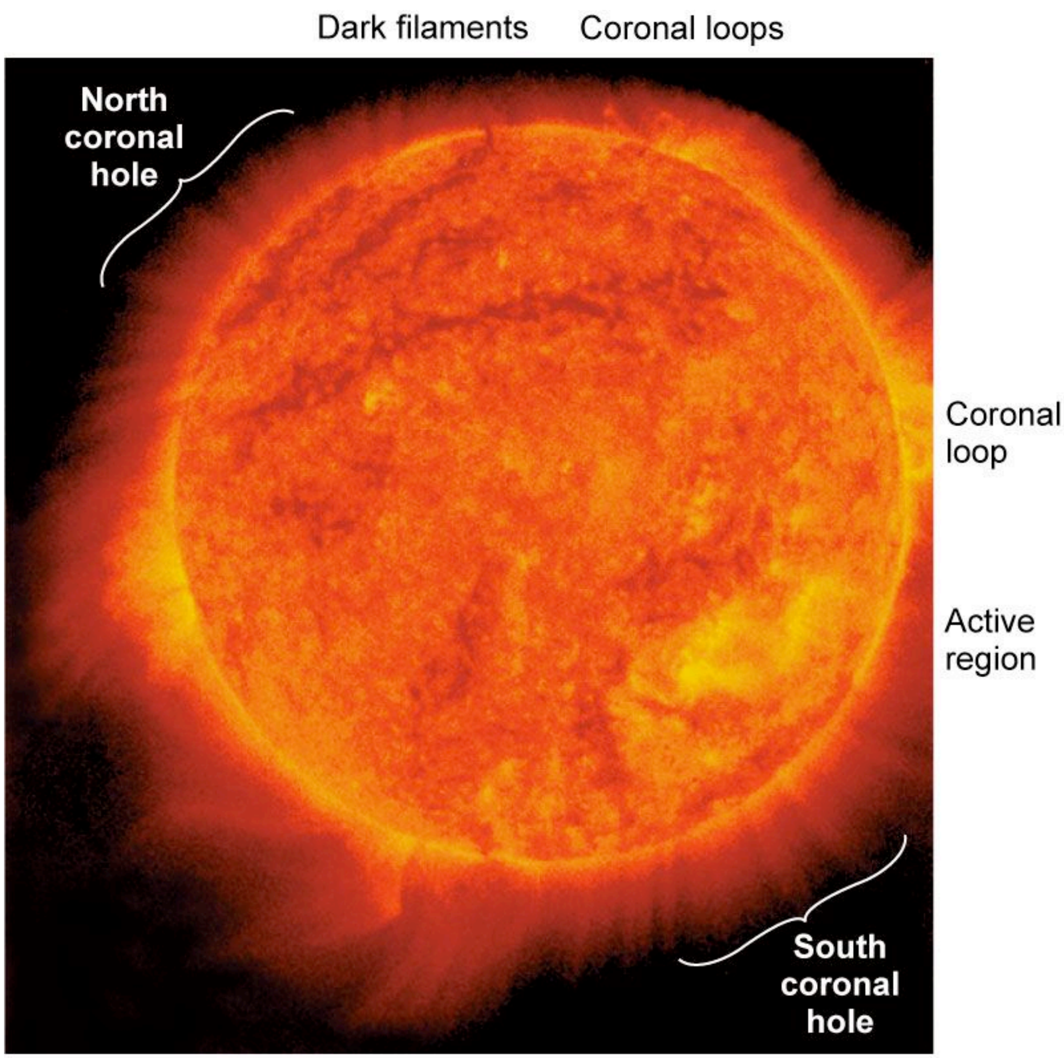

Courtesy of A.B.C. Walker (Stanford), T.W. Barbee (LLNL), R.B. Hoover and J.F. Lindbloom (NASA)

Colorplate IVa

The solar corona at 17.3 nm (71.7 eV), observed with a rocket launched Cassegrain telescope using Mo/Si coated mirrors ($d = 8.55$ nm, $\Gamma = 0.43$, 35% at 17.2 nm; Al L-edge filter at 72.5 eV narrows band pass to 17.1-17.5 nm, $\lambda/\Delta\lambda \simeq 40$). Emission dominated by Fe^{+8} and Fe^{+9} in the 100 eV (1.2×10^6 K) temperature coronal plasma.

Ch04_EUVastronomy.ai

EUV image of the solar corona showing loops near the solar limb

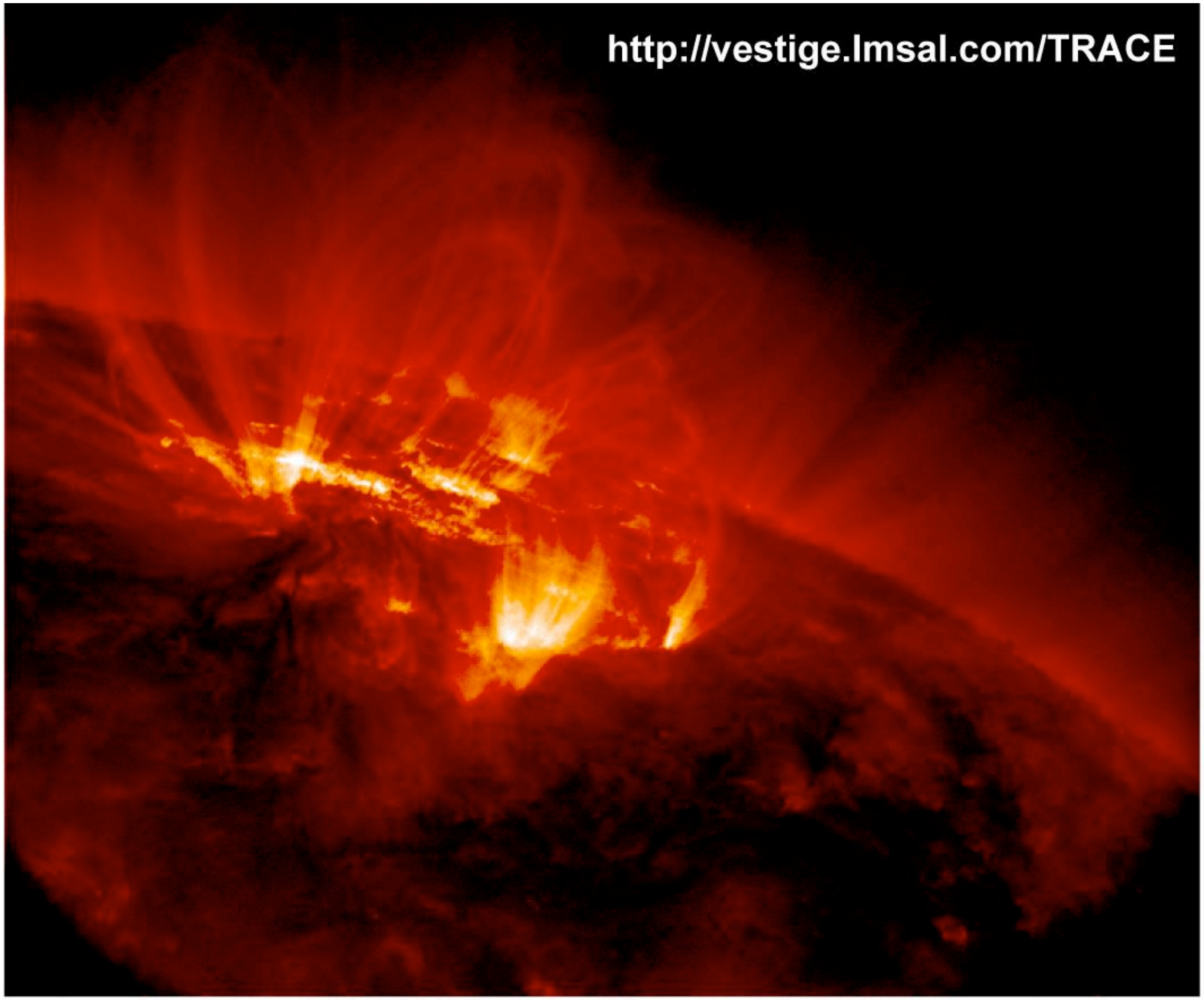

λ = 17.3 nm
(71.7 eV)

(Courtesy of L.Golub, Harvard-Smithsonian and T. Barbee, LLNL)

Ch04_F10VG_Sept05.ai

Dynamics of the solar corona

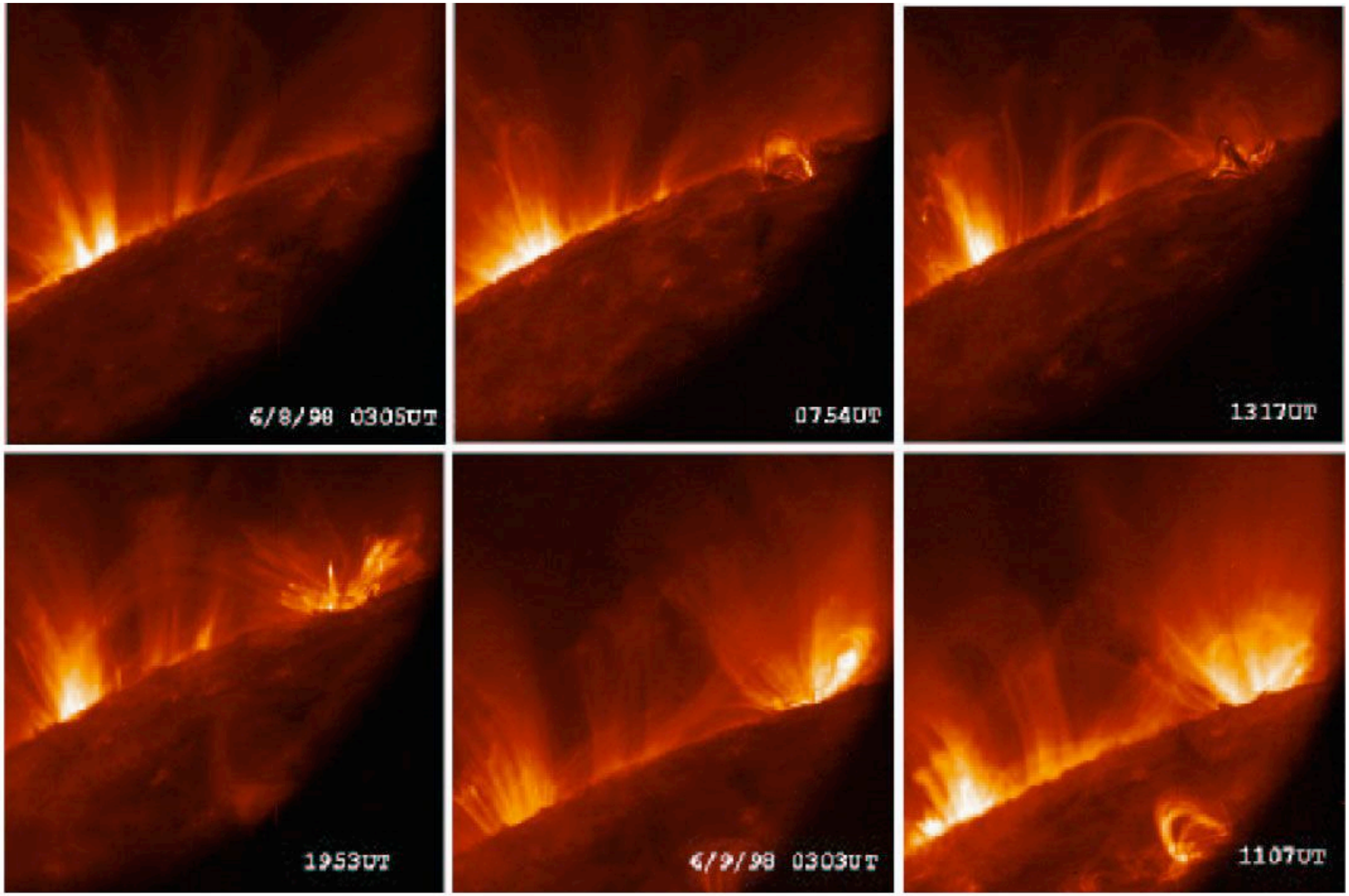

(Courtesy of L. Golub, Harvard-Smithsonian)

Ch04_DynamicsSolar.ai

Table 3.5. *Ionization potentials* (*electron volts*) [1–20].

Atom		Stage of ionization I	II	III	IV	V	VI	VII	VIII	IX	X	XI	XII	XIII	XIV
1	H	13.598 44													
2	He	24.587 41	54.417 78												
3	Li	5.391 72	75.640 18	122.454											
4	Be	9.322 63	18.211 16	153.897	217.713										
5	B	8.298 03	25.154 84	37.931	259.366	340.22									
6	C	11.260 30	24.383 32	47.888	64.492	392.08	489.98								
7	N	14.534 14	29.601 3	47.449	77.472	97.89	552.06	667.03							
8	O	13.618 06	35.117 30	54.936	77.413	113.90	138.12	739.29	871.41						
9	F	17.422 82	34.970 82	62.708	87.140	114.24	157.17	185.19	953.91	1 103.1					
10	Ne	21.564 54	40.963 28	63.45	97.12	126.21	157.93	207.28	239.10	1 195.8	1 362.2				
11	Na	5.139 08	47.286 4	71.620	98.91	138.40	172.18	208.50	264.25	299.9	1 465.1	1 648.7			
12	Mg	7.646 24	15.035 28	80.144	109.265	141.27	186.76	225.02	265.96	328.1	367.5	1 761.8	1 963		
13	Al	5.985 77	18.828 56	28.448	119.99	153.83	190.49	241.76	284.66	330.1	398.8	442.0	2 086	2 304	
14	Si	8.151 69	16.345 85	33.493	45.142	166.77	205.27	246.49	303.54	351.1	401.4	476.4	523	2 438	2 673
15	P	10.486 69	19.769 4	30.203	51.444	65.03	220.42	263.57	309.60	372.1	424.4	479.5	561	612	2 817
16	S	10.360 01	23.337 9	34.79	47.222	72.59	88.05	280.95	328.75	379.6	447.5	504.8	564	652	707
17	Cl	12.967 64	23.814	39.61	53.465	67.8	97.03	114.20	348.28	400.1	455.6	529.3	592	657	750
18	Ar	15.759 62	27.629 67	40.74	59.81	75.02	91.01	124.32	143.46	422.5	478.7	539.0	618	686	756
19	K	4.340 66	31.63	45.806	60.91	82.66	99.4	117.56	154.88	175.8	503.8	564.7	629	715	787
20	Ca	6.113 16	11.871 72	50.913	67.27	84.50	108.78	127.2	147.24	188.5	211.3	591.9	657	727	818
21	Sc	6.561 44	12.799 67	24.757	73.489	91.65	111.68	138.0	158.1	180.0	225.2	249.8	688	757	831
22	Ti	6.828 2	13.575 5	27.492	43.267	99.30	119.53	140.8	170.4	192.1	215.9	265.1	292	788	863
23	V	6.746 3	14.66	29.311	46.71	65.28	128.1	150.6	173.4	205.8	230.5	255.1	308	336	896
24	Cr	6.766 64	16.485 7	30.96	49.16	69.46	90.64	161.18	184.7	209.3	244.4	270.7	298	355	384
25	Mn	7.434 02	15.639 99	33.668	51.2	72.4	95.6	119.20	194.5	221.8	248.3	286.0	314	344	404
26	Fe	7.902 4	16.187 8	30.652	54.8	75.0	99.1	124.98	151.06	233.6	262.1	290.2	331	361	392
27	Co	7.881 0	17.083	33.50	51.3	79.5	103	131	160	186.2	276.2	305	336	379	411
28	Ni	7.639 8	18.168 84	35.19	54.9	75.5	108	134	164	193	224.6	321	352	384	430
29	Cu	7.726 38	20.292 40	36.841	55.2	79.9	103	139	167	199	232	266	369	401	435
30	Zn	9.394 05	17.964 40	39.723	59.4	82.6	108	136	175	203	238	274	311	412	454

Ar-like Fe
(26 – 8 = 18)

From: Allen's Astrophysical Quantities (Springer-Verlag, NY 1999), A. Cox, Editor.

Ch04_IonizatnChrt_Sept05.ai

IRON IX (Fe^{8+}), Z = 26
Ground State $1s^2 2s^2 2p^6 3s^2 3p^6 (^1S_0)$ (18 electrons)
Ionization Potential 1 884 000 cm^{-1}; 233.6 eV

Multiplet	Rel. Int.	λ_{vac} (in Å)	Levels (in 10^3 cm^{-1})	Configurations	Terms	J - J	Notes	References
	10	72.85	0.000 – 1372.67	$3s^2 3p^6 - 3s^2 3p^5 (^2P^\circ_{1/2}) 5s$	$g\,^1S - (\frac{1}{2},\frac{1}{2})^\circ$	0 – 1		009
		72.891	0.000 – 1371.9	$3s^2 3p^6 - 3s 3p^6 4p$	$g\,^1S - {}^1P^\circ$	0 – 1	A	440
	20	73.618	0.000 – 1358.36	$3s^2 3p^6 - 3s^2 3p^5 (^2P^\circ_{3/2}) 5s$	$g\,^1S - (\frac{3}{2},\frac{1}{2})^\circ$	0 – 1		729,9
	30	82.430	0.000 – 1213.15	$3s^2 3p^6 - 3s^2 3p^5 4d$	$g\,^1S - {}^1P^\circ$	0 – 1		241,9
	40	83.457	0.000 – 1198.22	$3s^2 3p^6 - 3s^2 3p^5 4d$	$g\,^1S - {}^3P^\circ$	0 – 1		241,9
	80	103.566	0.000 – 965.57	$3s^2 3p^6 - 3s^2 3p^5 (^2P^\circ_{1/2}) 4s$	$g\,^1S - (\frac{1}{2},\frac{1}{2})^\circ$	0 – 1		241,366
	60	105.208	0.000 – 950.500	$3s^2 3p^6 - 3s^2 3p^5 (^2P^\circ_{3/2}) 4s$	$g\,^1S - (\frac{3}{2},\frac{1}{2})^\circ$	0 – 1		241,366
	25	111.557	413.662 – 1310.15	$3s^2 3p^5 3d - 3s^2 3p^5 (^2P^\circ_{3/2}) 4f$	$^3P^\circ - \frac{3}{2}[\frac{7}{2}]$	2 – 3	Q	856
	10	111.713	405.765 – 1300.92	$3s^2 3p^5 3d - 3s^2 3p^5 (^2P^\circ_{3/2}) 4f$	$^3P^\circ - \frac{3}{2}[\frac{3}{2}]$	0 – 1		241,806
	20	111.791	408.307 – 1302.83	$3s^2 3p^5 3d - 3s^2 3p^5 (^2P^\circ_{3/2}) 4f$	$^3P^\circ - \frac{3}{2}[\frac{3}{2}]$	1 – 2		241,806
	40	112.017	408.307 – 1300.92	$3s^2 3p^5 3d - 3s^2 3p^5 (^2P^\circ_{3/2}) 4f$	$^3P^\circ - \frac{3}{2}[\frac{3}{2}]$	1 – 1		729
	40	112.096	413.662 – 1305.76	$3s^2 3p^5 3d - 3s^2 3p^5 (^2P^\circ_{3/2}) 4f$	$^3P^\circ - \frac{3}{2}[\frac{5}{2}]$	2 – 3	Q	241,806
	50	112.375	433.807 – 1323.65	$3s^2 3p^5 3d - 3s^2 3p^5 (^2P^\circ_{1/2}) 4f$	$^3F^\circ - \frac{1}{2}[\frac{5}{2}]$	2 – 3	Q	729
	20	113.793	425.800 – 1304.59	$3s^2 3p^5 3d - 3s^2 3p^5 (^2P^\circ_{3/2}) 4f$	$^3F^\circ - \frac{3}{2}[\frac{9}{2}]$	4 – 5		241,856
	40	114.024	429.311 – 1306.32	$3s^2 3p^5 3d - 3s^2 3p^5 (^2P^\circ_{3/2}) 4f$	$^3F^\circ - \frac{3}{2}[\frac{9}{2}]$	3 – 4		241,806
	20	114.111	433.807 – 1310.15	$3s^2 3p^5 3d - 3s^2 3p^5 (^2P^\circ_{3/2}) 4f$	$^3F^\circ - \frac{3}{2}[\frac{7}{2}]$	2 – 3		241,806
	30	115.353	456.744 – 1323.65	$3s^2 3p^5 3d - 3s^2 3p^5 (^2P^\circ_{1/2}) 4f$	$^1D^\circ - \frac{1}{2}[\frac{5}{2}]$	2 – 3		241,806
	30	115.996	462.609 – 1324.71	$3s^2 3p^5 3d - 3s^2 3p^5 (^2P^\circ_{1/2}) 4f$	$^3D^\circ - \frac{1}{2}[\frac{7}{2}]$	2 – 3		241,806

R.L. Kelly, Atomic and Ionic Spectrum Lines below 2000 Angstroms: Hydrogen through Krypton (AIP, NY, 1987)

Ch04_IronIXchrt.ai

IRON X (Fe^{9+}), Z = 26
Ground State $1s^2 2s^2 2p^6 3s^2 3p^5 (^2P^\circ_{3/2})$ (17 electrons)
Ionization Potential 2 114 000 cm^{-1}; 262.1 eV

Multiplet	Rel. Int.	λ_{vac} (in Å)	Levels (in 10^3 cm^{-1})	Configurations	Terms	J - J	Notes	References
		62.8	0. – 1592.4	$3s^2 3p^5 - 3s^2 3p^4 (^1D) 5s$	$g\,^2P^\circ - ^2D$	$\frac{3}{2} - \frac{5}{2}$		271
		75.685	0. – 1321.27	$3s^2 3p^5 - 3s^2 3p^4 (^1D) 4d$	$g\,^2P^\circ - ^2D$	$\frac{3}{2} - \frac{5}{2}$		241
		76.006	0. – 1315.69	$3s^2 3p^5 - 3s^2 3p^4 (^1D) 4d$	$g\,^2P^\circ - ^2P$	$\frac{3}{2} - \frac{3}{2}$		241
	30	76.495	15.6832 – 1322.96	$3s^2 3p^5 - 3s^2 3p^4 (^1D) 4d$	$g\,^2P^\circ - ^2D$	$\frac{1}{2} - \frac{3}{2}$		241,93
		76.53	0. – 1306.68	$3s^2 3p^5 - 3s^2 3p^4 (^1D) 4d$	$g\,^2P^\circ - ^2S$	$\frac{3}{2} - \frac{1}{2}$		271
	10	76.822	15.6832 – 1317.39	$3s^2 3p^5 - 3s^2 3p^4 (^1D) 4d$	$g\,^2P^\circ - ^2P$	$\frac{1}{2} - \frac{1}{2}$	P	856
	20	76.923	15.6832 – 1315.69	$3s^2 3p^5 - 3s^2 3p^4 (^1D) 4d$	$g\,^2P^\circ - ^2P$	$\frac{1}{2} - \frac{3}{2}$	P	856
		77.45	15.6832 – 1306.68	$3s^2 3p^5 - 3s^2 3p^4 (^1D) 4d$	$g\,^2P^\circ - ^2S$	$\frac{1}{2} - \frac{1}{2}$		271
		77.627	0. – 1288.21	$3s^2 3p^5 - 3s^2 3p^4 (^3P) 4d$	$g\,^2P^\circ - ^2F$	$\frac{3}{2} - \frac{5}{2}$		241
		77.728	0. – 1286.54	$3s^2 3p^5 - 3s^2 3p^4 (^3P) 4d$	$g\,^2P^\circ - ^4F$	$\frac{3}{2} - \frac{5}{2}$		241
		77.812	0. – 1285.18	$3s^2 3p^5 - 3s^2 3p^4 (^3P) 4d$	$g\,^2P^\circ - ^2D$	$\frac{3}{2} - \frac{3}{2}$		241
	20	77.865	0. – 1284.27	$3s^2 3p^5 - 3s^2 3p^4 (^3P) 4d$	$g\,^2P^\circ - ^2D$	$\frac{3}{2} - \frac{5}{2}$		241,93
		78.151	15.6832 – 1295.26	$3s^2 3p^5 - 3s^2 3p^4 (^3P) 4d$	$g\,^2P^\circ - ^2P$	$\frac{1}{2} - \frac{3}{2}$		241
	20	78.769	15.6832 – 1285.18	$3s^2 3p^5 - 3s^2 3p^4 (^3P) 4d$	$g\,^2P^\circ - ^2D$	$\frac{1}{2} - \frac{3}{2}$		241,93
	400	94.012	0. – 1063.69	$3s^2 3p^5 - 3s^2 3p^4 (^1D) 4s$	$g\,^2P^\circ - ^2D$	$\frac{3}{2} - \frac{5}{2}$		182
	100	95.338	0. – 1048.90	$3s^2 3p^5 - 3s^2 3p^4 (^3P) 4s$	$g\,^2P^\circ - ^2P$	$\frac{3}{2} - \frac{1}{2}$		182
	300	95.374	15.6832 – 1064.19	$3s^2 3p^5 - 3s^2 3p^4 (^1D) 4s$	$g\,^2P^\circ - ^2D$	$\frac{1}{2} - \frac{3}{2}$		182
	400	96.122	0. – 1040.35	$3s^2 3p^5 - 3s^2 3p^4 (^3P) 4s$	$g\,^2P^\circ - ^2P$	$\frac{3}{2} - \frac{3}{2}$		182

R.L. Kelly, Atomic and Ionic Spectrum Lines below 2000 Angstroms: Hydrogen through Krypton (AIP, NY, 1987)

Ch04_IronXchrt.ai

Extreme ultraviolet (EUV) lithography

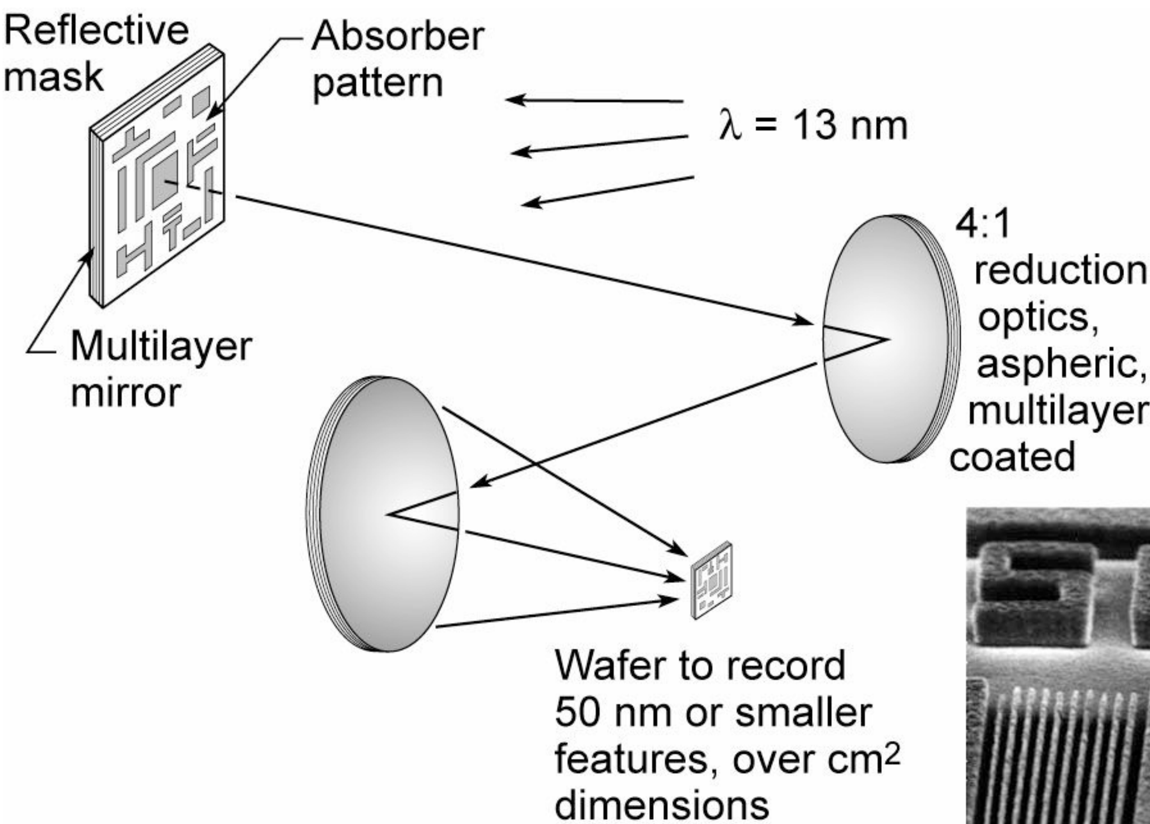

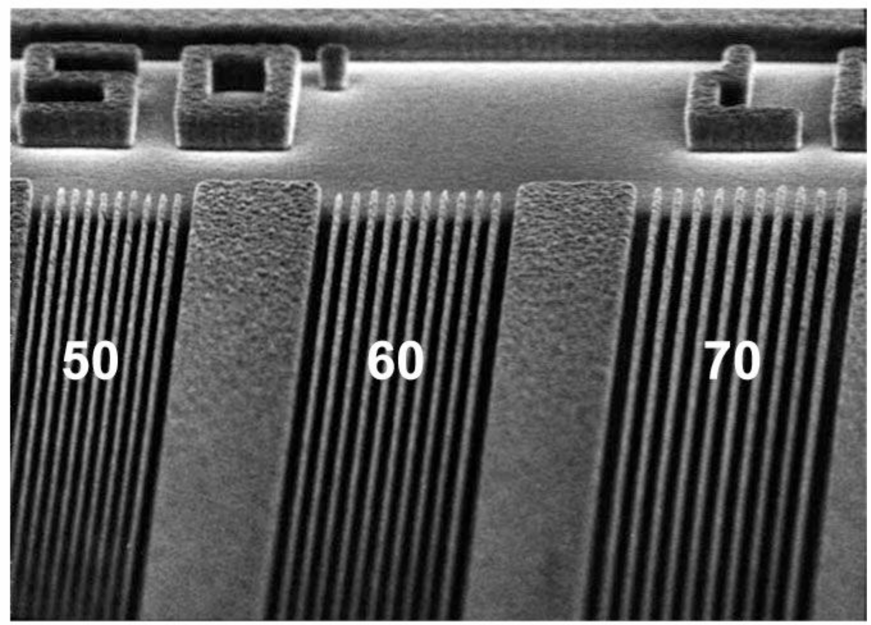

Ch04_F11VG.ai

Smooth multilayer coatings are required to minimize wavefront errors in EUV optical systems

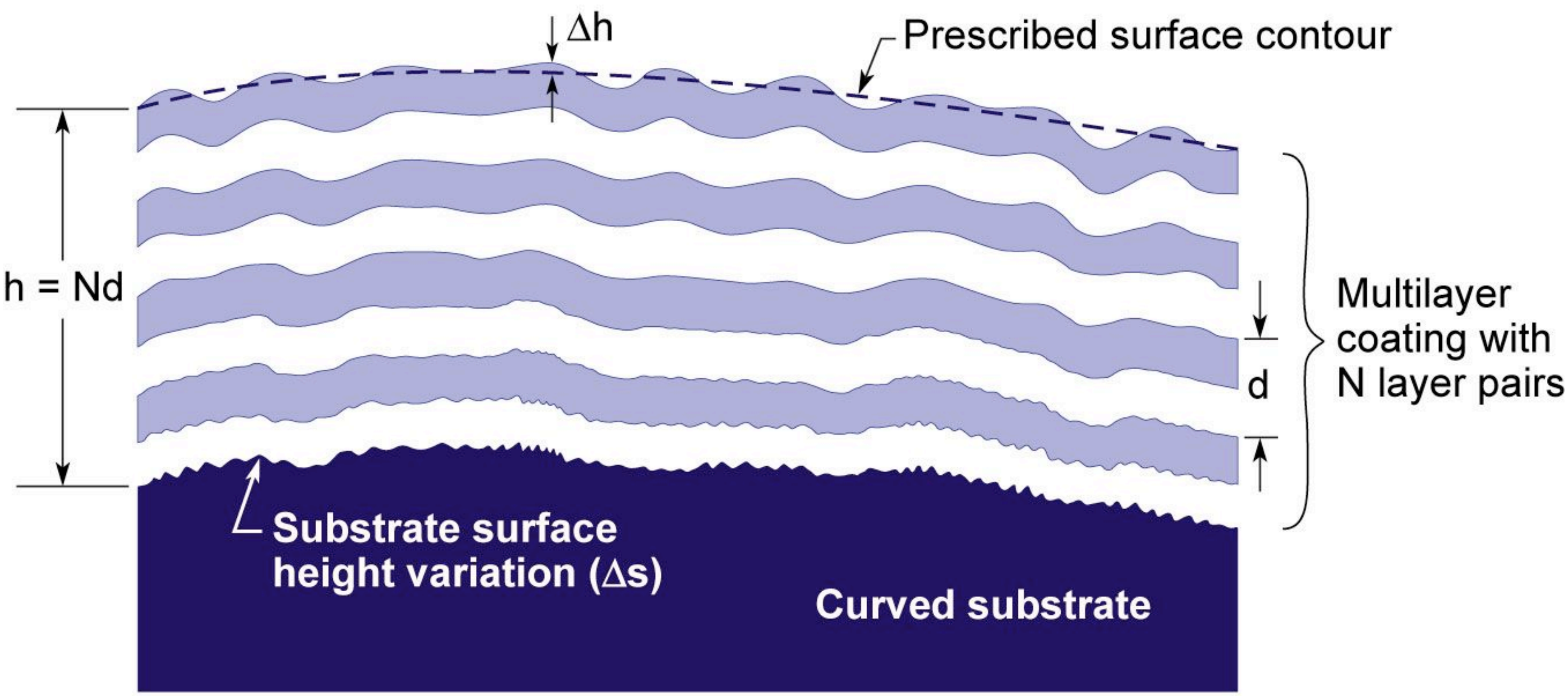

$$\Delta h = \frac{1}{2\sqrt{5}\sqrt{N_S}} \frac{\lambda}{25}$$

$$\frac{\Delta d}{d} = \frac{1}{25\sqrt{5}\sqrt{N_S}\,N}$$

- $\frac{\lambda}{25}$ total rms wavefront error
- $\Delta h_{rms} = \Delta s_{rms}/2$
- double path in reflection

Ch04_HW10.5.ai

Multilayer coatings for the ETS projection optics approach production specifications

Systematic d-space variations suggest path to further improvements.

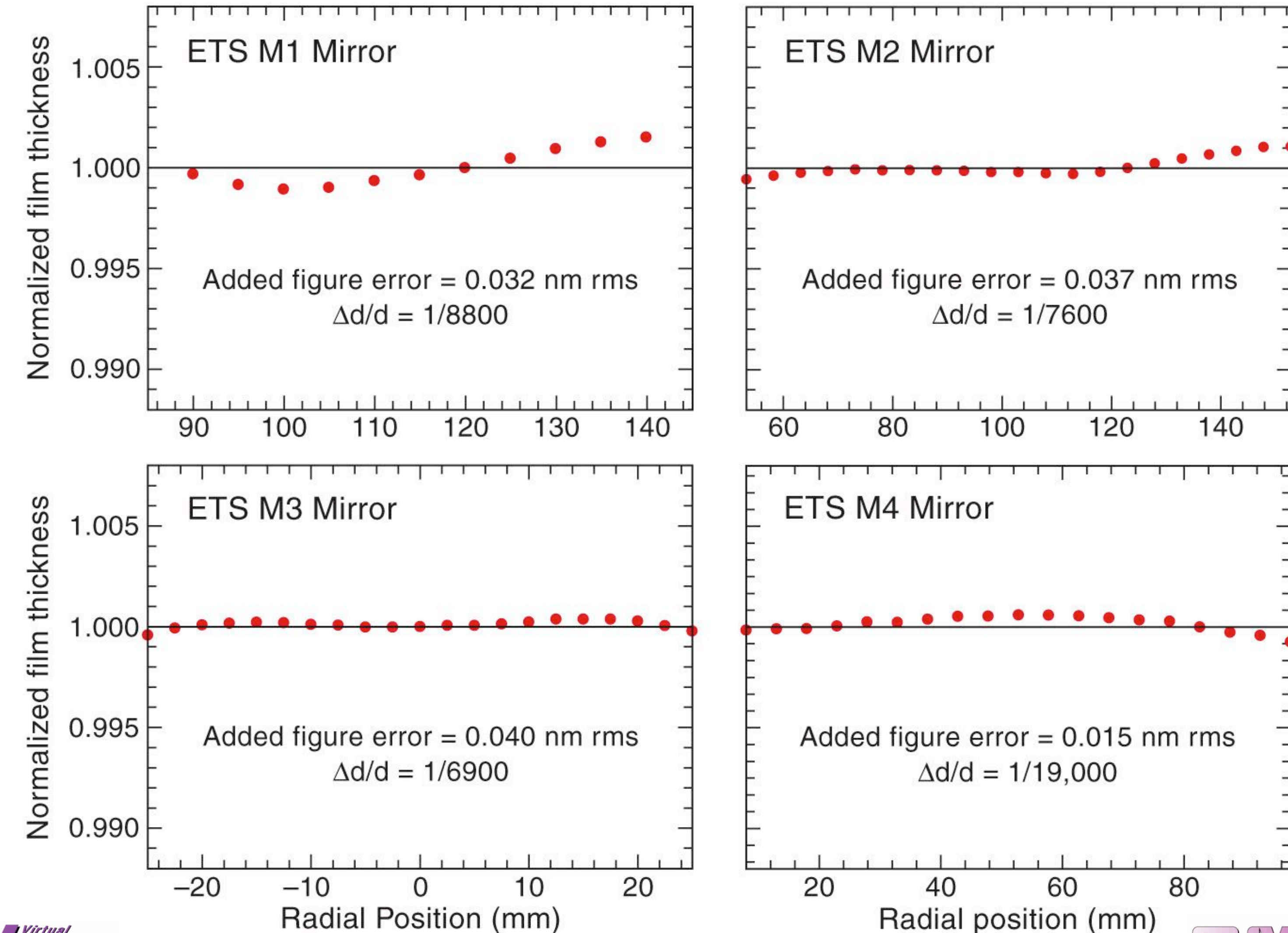

(Courtesy of R. Soufli and E. Spiller, LLNL)

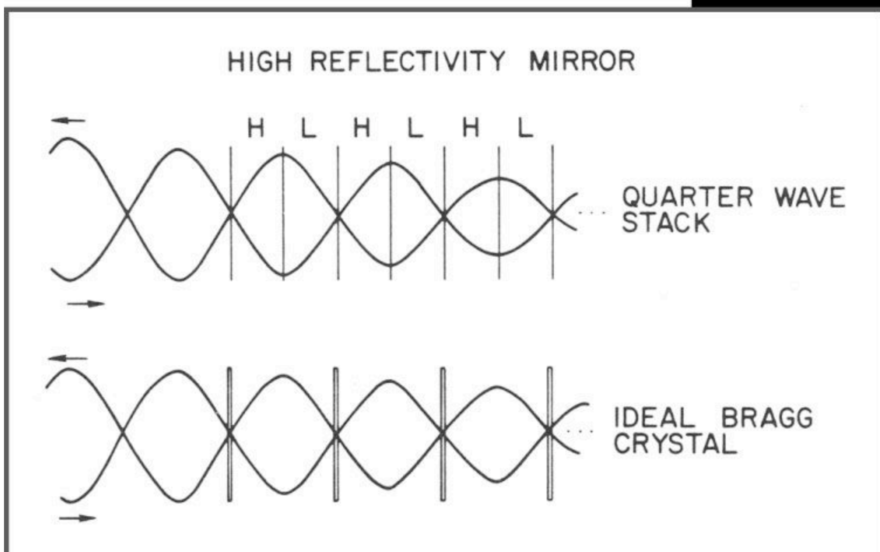

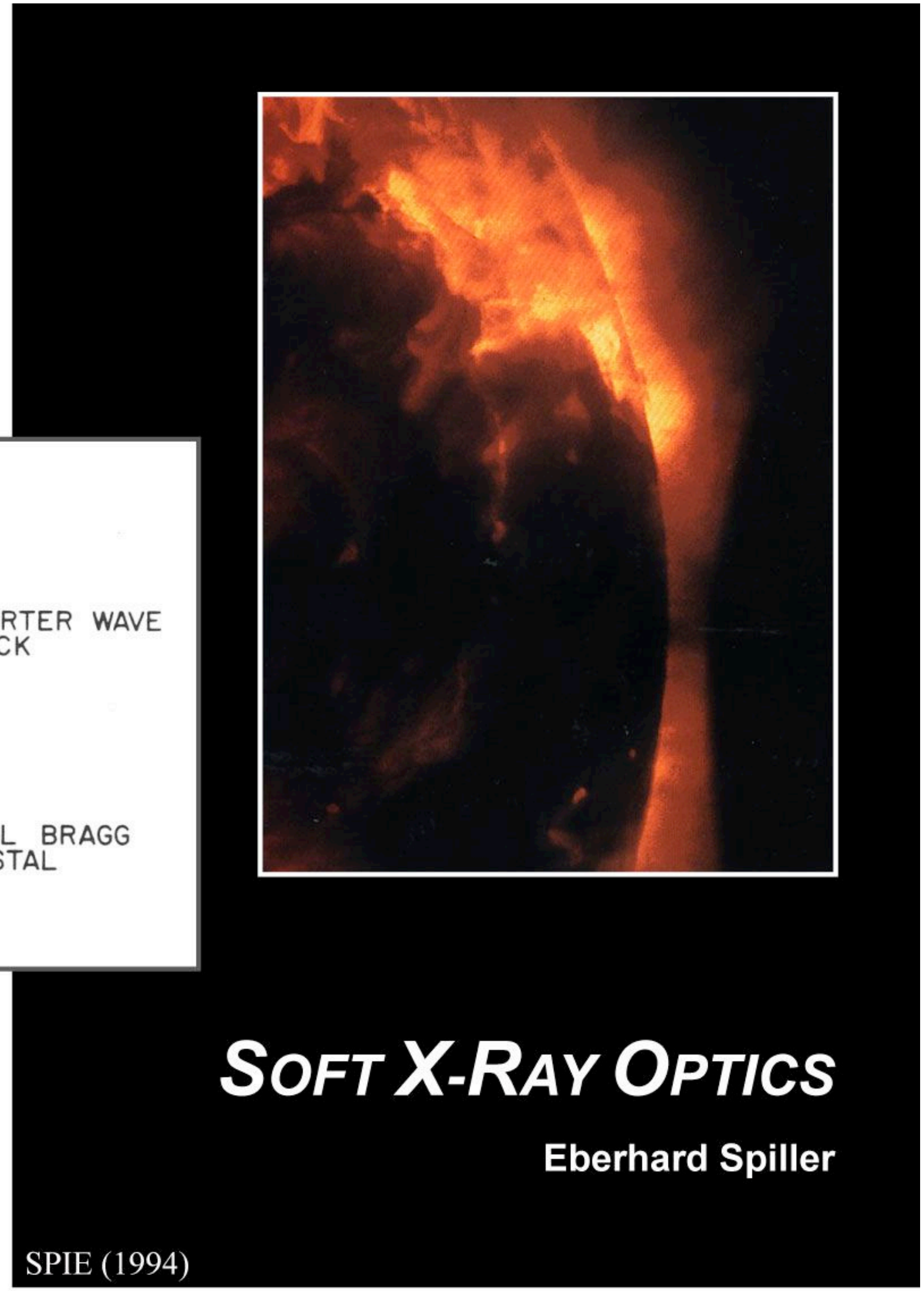

Ch04_SpillerBook.ai